

# Asian Anthropogenic Aerosol Forcing Played a Key Role in the Multidecadal Increase in Australian Summer Monsoon Rainfall

NORA L. S. FAHRENBACH<sup>a,b</sup>, MASSIMO A. BOLLASINA,<sup>a</sup> BJØRN H. SAMSET,<sup>c</sup> TIM COWAN<sup>d,e</sup>  
AND ANNICA M. L. EKMAN<sup>f</sup>

<sup>a</sup> School of GeoSciences, University of Edinburgh, Edinburgh, United Kingdom

<sup>b</sup> Institute for Atmospheric and Climate Science, ETH Zurich, Zurich, Switzerland

<sup>c</sup> Center for International Climate and Environmental Research (CICERO), Oslo, Norway

<sup>d</sup> Centre for Applied Climate Sciences, University of Southern Queensland, Toowoomba, Queensland, Australia

<sup>e</sup> Bureau of Meteorology, Melbourne, Victoria, Australia

<sup>f</sup> Department of Meteorology and Bert Bolin Centre for Climate Research, Stockholm University, Stockholm, Sweden

(Manuscript received 26 May 2023, in final form 7 November 2023, accepted 14 November 2023)

**ABSTRACT:** Observations show a significant increase in Australian summer monsoon (AUSM) rainfall since the mid-twentieth century. Yet the drivers of this trend, including the role of anthropogenic aerosols, remain uncertain. We addressed this knowledge gap using historical simulations from a suite of Coupled Model Intercomparison Project phase 6 (CMIP6) models, the CESM2 Large Ensemble, and idealized single-forcing simulations from the Precipitation Driver Response Model Intercomparison Project (PDRMIP). Our results suggest that Asian anthropogenic aerosol emissions played a key role in the observed increase in AUSM rainfall from 1930 to 2014, alongside the influence of internal variability. Sulfate aerosol emissions over Asia led to regional surface cooling and strengthening of the climatological Siberian high over eastern China, which altered the meridional temperature and sea level pressure gradients across the Indian Ocean. This caused an intensification and southward shift of the Australian monsoonal westerlies (and the local Hadley cell) and resulted in a precipitation increase over northern Australia. Conversely, the influence of increased greenhouse gas concentrations on AUSM rainfall was minimal due to the compensation between thermodynamically induced wettening and transient eddy-induced drying trends. At a larger scale, aerosol and greenhouse gas forcing played a key role in the climate response over the Indo-Pacific sector and eastern equatorial Pacific, respectively (coined the “tropical Pacific east–west divide”). These findings contribute to an improved understanding of the drivers of the multidecadal trend in AUSM rainfall and highlight the need to reduce uncertainties in future projections under different aerosol emission trajectories, which is particularly important for northern Australia’s agriculture.

**SIGNIFICANCE STATEMENT:** Australian summer monsoon (AUSM) rainfall plays a vital role in sustaining northern Australia’s unique biodiversity and extensive agricultural industry. While observations show a significant increase in AUSM rainfall since the mid-twentieth century, the causes remain uncertain. We find that anthropogenic aerosol emissions from Asia played a key role in driving this multidecadal AUSM rainfall trend by inducing dynamic adjustments over the Indo-Pacific sector. These findings highlight the need to consider different aerosol emission trajectories when assessing future projections of AUSM rainfall.


**KEYWORDS:** Atmospheric circulation; Australia; Monsoons; Precipitation; Anthropogenic effects/forcing; Aerosols/particulates


## 1. Introduction

Australian precipitation varies strongly in both space and time, with around 80% of the total annual rainfall over tropical northern Australia (NA; Australian land region north of

20°S) occurring as part of the Australian summer monsoon (AUSM) (Nicholls et al. 1997; Gutiérrez et al. 2021a). The AUSM arises from the southward movement of the intertropical convergence zone (ITCZ) and shift of the Hadley circulation during austral summer (Gadgil 2018). The AUSM typically onsets in December (Lisonbee et al. 2019), with the reversal of lower-tropospheric winds from easterly to westerly, and withdraws in early March (Drosowsky 1996; Suppiah 1992). It is vital for sustaining NA’s unique biodiversity (Bowman 2002) and extensive agricultural industries (Suppiah 1992; McKeon et al. 2021).

A significant increase in AUSM rainfall, particularly over northwest Australia (NWA; land area bounded by 10°–20°S, 110°–135°E), and an associated strengthening of the monsoonal flow have been observed since the mid-twentieth century (Taschetto and England 2009; Dey et al. 2019; Dai 2021).

 Denotes content that is immediately available upon publication as open access.

 Supplemental information related to this paper is available at the Journals Online website: <https://doi.org/10.1175/JCLI-D-23-0313.s1>.

*Corresponding author:* Nora L. S. Fahrenbach, [nora.fahrenbach@env.ethz.ch](mailto:nora.fahrenbach@env.ethz.ch); [n.l.s.fahrenbach@sms.ed.ac.uk](mailto:n.l.s.fahrenbach@sms.ed.ac.uk)

DOI: 10.1175/JCLI-D-23-0313.1

© 2024 American Meteorological Society. This published article is licensed under the terms of a Creative Commons Attribution 4.0 International (CC BY 4.0) License



This long-term trend was found to be highly unusual in the multicentury context of paleoclimate reconstructions (Freund et al. 2017). However, its driving mechanisms remain unclear (Dey et al. 2019; Heidemann et al. 2022), hindered partly by the significant influence of climate variability (e.g., Power et al. 1999).

Previous studies reported a detectable anthropogenic signal in the NWA precipitation increase (Frederiksen and Grainger 2015; Knutson and Zeng 2018). The greenhouse gas (GHG)-induced warming of the tropical Atlantic Ocean has been proposed to contribute by generating an eastward traveling Rossby wave train leading to subsequent upper-tropospheric divergence over NWA (Lin and Li 2012). Another potential mechanism is related to the GHG-induced expansion of the Indo-Pacific warm pool which leads to an increased duration of the Madden–Julian oscillation (MJO) active phases over the Maritime Continent by 5–6 days since the 1980s, resulting in wetter anomalies across the region (Roxy et al. 2019; Borowiak et al. 2023). In contrast, Cao et al. (2023) attributed the Australian monsoon precipitation to changes in the Southern Hemisphere (SH) monsoon circulation, primarily linked to the sea surface temperature (SST) gradient between the eastern Pacific and Indo-Pacific Ocean.

Anthropogenic aerosols have also been proposed as a potential driver for the NWA rainfall increase (Rotstayn et al. 2007, 2012; Dey et al. 2019). Aerosols can perturb Earth's radiation budget directly by reflecting or absorbing incoming solar radiation (aerosol–radiation interactions; e.g., Szopa et al. 2021) and indirectly by modifying cloud properties and precipitation (aerosol–cloud interactions; Twomey 1977; Albrecht 1989). These different aerosol effects can further induce circulation adjustments, both locally and remotely to the aerosol emission region, resulting in complex impacts on temperature profiles and precipitation patterns (e.g., Ming and Ramaswamy 2009; Lewinschal et al. 2013; Wilcox et al. 2019). Aerosols have been previously found to play a key role in driving the decrease in Sahel rainfall (e.g., Biasutti and Giannini 2006) and changes in regional (e.g., Wang et al. 2009; Bollasina et al. 2011; Westervelt et al. 2020) and global monsoons (e.g., Shonk et al. 2020) as well as the tropical rain belt (e.g., Allen et al. 2014). Over the Northern Hemisphere (NH), anthropogenic aerosols have exerted a suppressing effect on monsoon precipitation from 1901 to 2014, which has been attributed to a decrease in surface evaporation as well as weakening of the monsoon circulation, closely linked to a reduced interhemispheric temperature gradient (Cao et al. 2022a). Yet, the complexity of aerosol–climate interactions contributes significantly to the uncertainty in estimates of the present-day radiative forcing (Szopa et al. 2021).

Rotstayn et al. (2007, 2012) used the ocean–atmosphere climate models CSIRO-Mk3 and CSIRO-Mk3.6, respectively, to investigate the role of anthropogenic aerosols and GHGs on the NWA wetting since the 1950s. They found this trend to be reproducible only when including anthropogenic aerosol forcing, primarily due to the Asian aerosol haze, which altered the meridional temperature and pressure gradients across the Indian Ocean and strengthened the monsoonal flow toward NWA. These aerosol-induced changes may have masked the GHG-related effects on rainfall and circulation

over the Indo-Pacific sector, although the underlying physical mechanism remained uncertain (Rotstayn et al. 2007, 2012). However, some caveats of the studies were the simplified treatment of aerosol processes, the lack of model agreement with observations over other parts of Australia than NWA, and the model's inability to correctly simulate interdecadal and longer variability in Australian rainfall (Rotstayn et al. 2007, 2012). Shi et al. (2008) showed that the NWA rainfall increase in the low-resolution CSIRO-Mk3 resulted from the model's unrealistic westward extension of the Pacific SST cold tongue, with large warming in the eastern Indian Ocean driving a positive NWA rainfall anomaly. Cai et al. (2011) found that none of the multimodel ensemble averages across 24 models from phase 3 of the Coupled Model Intercomparison Project (CMIP3) could reproduce the observed wetting over NWA. These models either included both the direct and indirect aerosol effect or only the direct aerosol effect, suggesting that aerosol forcing played a negligible role in this wetting trend. In contrast, Dey et al. (2019) found that aerosol-only simulations across a suite of CMIP5 models better captured the observed trends than GHG- and natural forcing-only simulations, providing evidence to support the link between NWA rainfall and aerosol increases. However, reservations regarding these conclusions stem from differences between the simulated and observed magnitude and pattern of precipitation trends over Australia (Dey et al. 2019) as well as a missing investigation of the influence of model biases (like the cold tongue bias) on the simulated precipitation pattern.

To date, the cause of the long-term increase in AUSM rainfall, including the role of anthropogenic aerosols, remains uncertain (Heidemann et al. 2023). We tackle this knowledge gap using a suite of CMIP6 models, large-ensemble simulations, and idealized GHG and aerosol simulations to 1) quantify the contribution of anthropogenic forcing against the background of internal variability, 2) identify the geographical location of the dominant aerosol source region influencing the NA precipitation trend, and 3) provide an improved understanding of the underpinning physical mechanism. Answering these questions will advance our fundamental understanding of long-term changes in the Australian hydrological cycle and provide a framework to more robustly constrain and reduce currently large uncertainties in future projections of AUSM rainfall (Brown et al. 2016; Narsey et al. 2020).

## 2. Data and methods

### a. Observations and reanalysis data

We use monthly gridded land precipitation data from the Global Precipitation Climatology Centre (GPCC v2022; Schneider et al. 2022) at a  $0.5^\circ \times 0.5^\circ$  horizontal resolution to investigate multidecadal precipitation variations over tropical NA (Australian land region north of  $20^\circ\text{S}$ ; box in Fig. 1c). Note that we are using “NA” when referring to the Australian region and “AUSM” when discussing the seasonality or timing of the rainfall. Our analysis focuses on the austral summer [December–February (DJF)] trend from 1930 to 2014, which is statistically significant at the



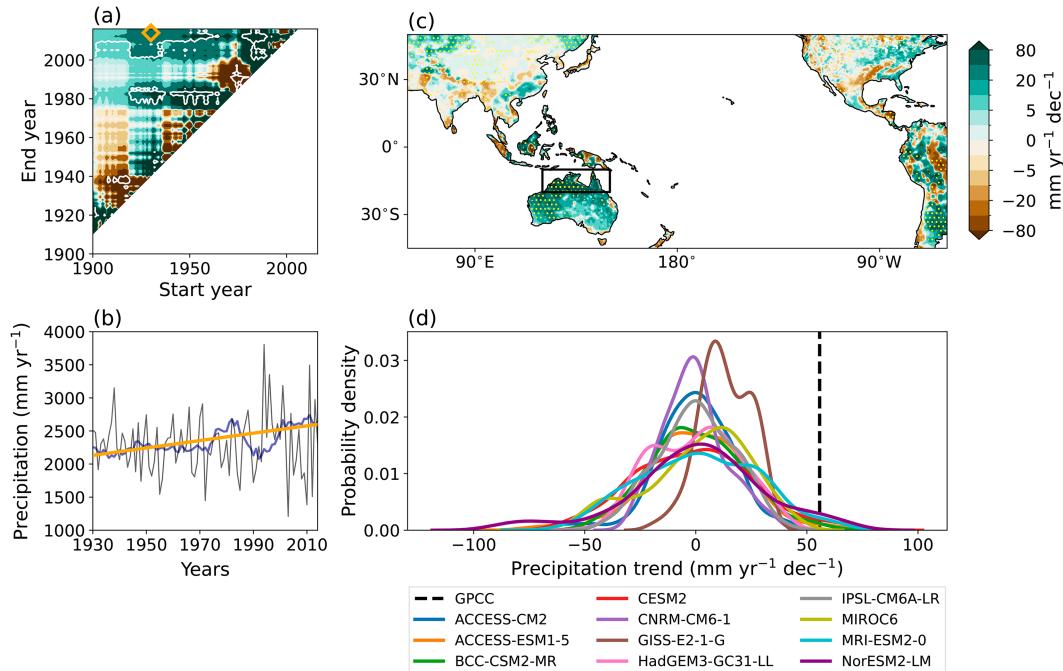


FIG. 1. (a) Observed DJF precipitation trends over northern Australia (box in Fig. 1c) as a function of the start and end years in the twentieth century, based on GPCC observational data. All trends with a minimum length of 10 years are shown. The orange diamond marks the 1930–2014 trend analyzed in this study. Significance at the 90% confidence level according to a Student’s  $t$  test is shown by white contours. (b) Unsmoothed (gray) and 11-yr running mean (blue) time series of area-averaged DJF precipitation over northern Australia. The orange line shows the least squares linear trend between 1930–2014. (c) Spatial distribution of least squares linear trend of observed DJF precipitation over the period 1930–2014. The black box shows the northern Australia region ( $10^{\circ}$ – $20^{\circ}$ S,  $120^{\circ}$ – $150^{\circ}$ E; land only). Stippling indicates significance at the 90% confidence level. (d) Kernel probability density distribution of 85-yr-long DJF precipitation trends over northern Australia as determined using the preindustrial control simulations from 11 CMIP6 models. The dashed line shows the observed 1930–2014 trend analyzed in this study.

90% level using a two-tailed Student’s  $t$  test (Fig. 1). This period is chosen to focus on multidecadal historical trends in AUSM rainfall and thus allows us to identify anthropogenic forcing signals beyond the influence of internal variability. A sensitivity analysis to the length of the period shows results to be robust (see discussion in section 3a). A comparison between GPCC and other gauge-only datasets from the Climate Research Unit (CRU TS v4; Harris et al. 2020) and the Australian Bureau of Meteorology (AWAP; Jones et al. 2009) shows high spatial and temporal agreement over Australia from 1930 to 2014 (Fig. S1 in the online supplemental material), although this can be partly explained by the use of AWAP data to derive GPCC and CRU datasets (Harris et al. 2020; Schneider et al. 2022).

To identify observed changes in near-surface climate associated with the AUSM rainfall trend, we use monthly SST data at a  $1^{\circ}$  resolution from the Hadley Centre Global Sea Ice and Sea Surface Temperature dataset (HadISST v1.1; Hadley Centre for Climate Prediction and Research 2007) as well as monthly near-surface temperature, mean sea level pressure, and wind data at a  $1^{\circ}$  resolution from the NOAA–CIRES–DOE Twentieth Century Reanalysis Project (20CRv3; Slivinski et al. 2019).

#### b. Historical and preindustrial CMIP6 simulations

We examine the role of anthropogenic forcing on the AUSM rainfall trend using output from 11 state-of-the-art CMIP6 models with 3–10 ensemble members each (Table 1). These models were selected based on the availability of historical all-forcing (hereafter hist-All), GHG-only (hereafter hist-GHG), and anthropogenic aerosol-only (hereafter hist-AER) simulations in order to keep consistency across the various multimodel ensemble means (MEMs). The MEMs were calculated by computing the ensemble mean for each model first and then averaging these after interpolating each model data to a common  $2.5^{\circ} \times 2^{\circ}$  grid. This use of MEMs reduces uncertainties related to internal climate variability and provides a more robust estimate of the forced climate response. The MEM captures the observed climatological precipitation pattern in DJF over Australia well, although it underestimates precipitation along the northern and eastern coastlines (Fig. S2).

To assess whether the 1930–2014 rainfall trend over NA lies outside the bounds of internal climate variability, we analyze the corresponding preindustrial control runs (Eyring et al. 2016) with at least 500 simulated years for each model. We construct probability density functions (PDFs) from 85-yr running mean trends for each model using kernel density

TABLE 1. List of the CMIP6 models used in this study that performed the required hist-All, hist-GHG, and hist-AER simulations. The number of ensemble members, horizontal resolution, aerosol forcing, and, where applicable, the aerosol component are given (Gutiérrez et al. 2021b).

Model name	Ensembles	Horizontal resolution	Aerosol forcing and component
ACCESS-CM2	3	1.9° × 1.3°	Interactive, UKCA-GLOMAP
ACCESS-ESM-1-5	3	1.9° × 1.3°	Interactive, CLASSIC (v1.0)
BCC-CSM2-MR	3	1.1° × 1.1°	Prescribed from MACv2-SP
CESM2	3	1.3° × 0.9°	Interactive, MAM4
CNRM-CM6-1	10	1.4° × 1.4°	Prescribed from TACTIC_v2
GISS-E2-1-G	10	2.5° × 2.0°	Prescribed from NINT
HadGEM3-GC31-LL	5	1.9° × 1.3°	Interactive, U.K.-GLOMAP
IPSL-CM6A-LR	10	2.5° × 1.3°	Prescribed from INCA
MIROC6	10	1.4° × 1.4°	Interactive, SPRINTARS
MRI-ESM2-0	5	1.1° × 1.1°	Interactive, MASINGAR mk-2r4c
NorESM2-LM	3	2.5° × 1.9°	Interactive, OsloAero6

estimates and compare these distributions to the observed precipitation trend.

We further utilize Large Ensemble simulations from the Community Earth System Model version 2 (CESM2 Large Ensemble; Rodgers et al. 2021) to separate the influence of internal variability and anthropogenic forcing on the wetting trend over NA. A detailed description of the model configuration and simulations is given in section 3 of the online supplemental material.

### c. Moisture budget decomposition

To examine the physical mechanism driving the AUSM rainfall trend, we analyze trends in the components of the moisture budget for the historical all- and single-forcing CMIP6 simulations using a simplified method adapted from Seager et al. (2010). The moisture budget equation is given by

$$\Delta(P - E) \approx \Delta\text{TH} + \Delta\text{MCD} + \Delta\text{TE}, \quad (1)$$

where values of precipitation  $P$  and evaporation  $E$  can be obtained directly from the model output. The thermodynamic term  $\Delta\text{TH}$  involves precipitation changes arising only from changes in the specific humidity, the dynamic term  $\Delta\text{MCD}$  involves precipitation changes arising only from changes in the mean atmospheric circulation, and the transient eddy term  $\Delta\text{TE}$  involves precipitation changes from covarying changes in humidity and mean circulation. The terms  $\Delta\text{TH}$  and  $\Delta\text{MCD}$  can be evaluated using

$$\Delta\text{TH} = -\frac{1}{\rho_w g} \int_{p_{\text{TOA}}}^{p_s} \nabla \cdot [\mathbf{u}_c(\Delta q)] dp, \quad \text{and} \quad (2)$$

$$\Delta\text{MCD} = -\frac{1}{\rho_w g} \int_{p_{\text{TOA}}}^{p_s} \nabla \cdot [(\Delta \mathbf{u})q_c] dp, \quad (3)$$

where  $\rho_w$  is the density of water,  $g$  is the gravitational acceleration,  $p_s$  is the pressure at the surface,  $p_{\text{TOA}}$  is the pressure at the top of the atmosphere,  $\mathbf{u}$  is the horizontal wind vector, and  $q$  is the specific humidity. The DJF 1930–2014 trends of the quantities are denoted by  $\Delta$  and the subscript  $c$  indicates climatological mean values between 1920 and 1940 (note that choosing 1930–2014 as the climatological reference period or

using period differences gives nearly identical results). For the all- and single-forcing historical simulations, we calculate the terms  $\Delta(P - E)$ ,  $\Delta\text{TH}$ , and  $\Delta\text{MCD}$  for each model and approximate  $\Delta\text{TE}$  as the residual from Eq. (1) [as done by, e.g., Chung et al. (2014)] as no daily data are available for all models for a direct evaluation. The MEM is then calculated by interpolating to a common 2.5° × 2° grid and averaging across the 10 models (note that CESM2 did not provide all the relevant data).

### d. PDRMIP simulations

Simulations from PDRMIP (Precipitation Driver Response Model Intercomparison Project; Myhre et al. 2017b) are used to corroborate the analysis of the historical CMIP6 simulations regarding the influence of anthropogenic forcing and, in particular, to identify the dominant aerosol species and source region influencing NA precipitation. We focus on the experiments driven by a global doubling of the CO<sub>2</sub> concentrations (hereafter CO<sub>2</sub> × 2) relative to the year 2000, a fivefold increase in sulfate concentrations or emissions (hereafter SUL × 5) and a tenfold increase in black carbon concentrations or emissions (hereafter BC × 10) as well as a tenfold increase in sulfate concentrations or emissions over Asia (10°–50°N, 60°–140°E; hereafter SUL × 10Asia), a tenfold increase in sulfate concentration or emissions over Europe (35°–70°N, 10°–40°E; hereafter SUL × 10Eur), and a tenfold increase in black carbon concentration or emissions over Asia (hereafter BC × 10Asia) relative to the year 2000 baseline. The simulated step perturbation and equilibrium response differs from real-world transient adjustments but allows a clearer emergence of the signal from internal variability for sufficiently large forcing. We remapped the output to a common 2.5° × 2.5° grid and focused on the multimodel means across nine and six CMIP5-generation models from PDRMIP that performed the global and regional perturbation simulations, respectively (Table S2).

For the perturbation and baseline experiments, the models were run for 15 years with fixed SST and for 100 years with slab or fully coupled ocean simulations. We use the former simulations to diagnose fast precipitation responses ( $\Delta P_{\text{fast}}$ ), which refer to rapid climate adjustments scaling with changes

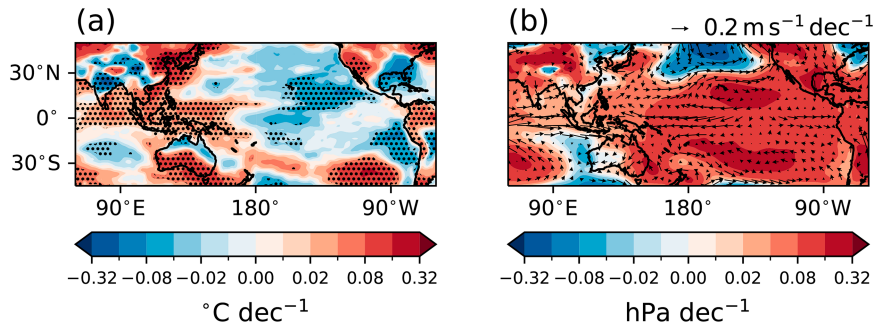


FIG. 2. Spatial distribution in trends over 1930–2014 for DJF (a) near-surface temperature from the Twentieth Century Reanalysis Project over land (Slivinski et al. 2019) and SSTs from HadISST (Hadley Centre for Climate Prediction and Research 2007) after removing the tropical mean trend (25°N–25°S) and (b) mean sea level pressure (colors) with 850-hPa winds (vectors) from the Twentieth Century Reanalysis Project (Slivinski et al. 2019). Stippling in (a) shows significance at the 90% level using the two-tailed Student's  $t$  test.

in atmospheric absorption (e.g., Myhre et al. 2013). We use the coupled simulations to analyze the total precipitation response ( $\Delta P_{\text{total}}$ ) due to both fast and slow (i.e., climate response scaling with changes in oceanic temperature) adjustments. The slow response ( $\Delta P_{\text{slow}}$ ) can then be computed as

$$\Delta P_{\text{slow}} = \Delta P_{\text{total}} - \Delta P_{\text{fast}}, \quad (4)$$

assuming that the total response is given by a linear combination of the fast and slow response (Samset et al. 2016; Liu et al. 2019). Our analysis focuses on years 3–15 of the fixed SST simulations and years 51–100 of the coupled simulations. All responses are given as the difference between the perturbation and control simulations.

### 3. Results

#### a. Observed trend and variability of AUSM rainfall

Figure 1a shows the observed austral summer (DJF) rainfall trend over NA as a function of the start and end years during the twentieth century. A significant influence of internal variability is evident as shown by the frequent shifts between drying and wetting periods on decadal and longer time scales. However, a distinct multidecadal to centennial wetting trend is clearly identifiable. This sign of this trend is independent of the choice of the start year and robust with variations of the end year after the 1980s, being statistically significant at the 90% level for end years between 2005 and 2014. Our study focused on the 1930–2014 precipitation trend over NA to examine long-term changes driven by the AUSM (Figs. 1b,c). Note that this trend clearly stands out as one of the largest within the tropics and subtropics (Fig. 1c).

To further analyze the trend in the context of multidecadal variability, we constructed frequency distributions of the 85-yr running trends for the CMIP6 model output (Fig. 1d). Despite intermodel differences in the shape and maximum values of the individual curves, the observed 1930–2014 trend lies at the upper tail (i.e., above the 95th percentile) of the preindustrial control distributions of all models. The trend even lies above

the 99th percentile and outside the PDFs for five and two (i.e., CNRM-CM6-1 and GISS-E2-1-G) of those models, respectively. This indicates that the trend is unlikely due to internal variability alone but predominantly externally forced.

The increasing AUSM precipitation trend is associated with distinct large-scale features in temperature, mean sea level pressure and circulation. In particular, the near-surface and SST temperatures (after subtracting the tropical mean trend between 25°N–25°S) show a significant widespread cooling in the central-eastern tropical Pacific, a tropical Indian Ocean warming, and statistically significant cooling over eastern Asia compared to the tropical mean temperatures (Fig. 2a). A trend toward higher mean sea level pressure over China and a meridional gradient across the Indian Ocean are evident (Fig. 2b). The observed trend in 850-hPa wind shows strengthened and southward-shifted monsoonal westerly flow over the Indian Ocean, channeled toward NWA by a low pressure trend off the coast of Western Australia (Fig. 2b). These moisture-laden winds result in the observed precipitation increase over NA (Fig. 1c).

#### b. Simulation and attribution of AUSM rainfall increase

##### 1) HISTORICAL TRENDS IN CMIP6 SIMULATIONS

The hist-All MEM captures the wetting trend over NA and the rest of the continent well (Figs. 1c and 3a), albeit with a weaker magnitude (MEM value of  $12 \text{ mm yr}^{-1} \text{ decade}^{-1}$ ) compared to observations (mean value of  $55.7 \text{ mm yr}^{-1} \text{ decade}^{-1}$ ). Over the central and eastern equatorial Pacific, the hist-All ensemble shows increased precipitation over the ITCZ core region (Fig. 3a and 4b). A large part of this  $\Delta(P - E)$  pattern can be attributed to changes in the mean circulation dynamics  $\Delta\text{MCD}$  (Figs. 5a,c), such as the anomalous low-level convergence (Fig. 3e) and associated midtropospheric ascent (Fig. 3d), which leads to the wetting trend over the ITCZ core (Figs. 3a and 4b). Together with the pattern of anomalous subsidence over the Maritime Continent (Fig. 3d) and the lower-tropospheric velocity potential zonal dipole (Fig. 3e), this circulation pattern opposes the climatological flow and suggests a weakening of the Indo-Pacific Walker circulation with ensuing El Niño-like



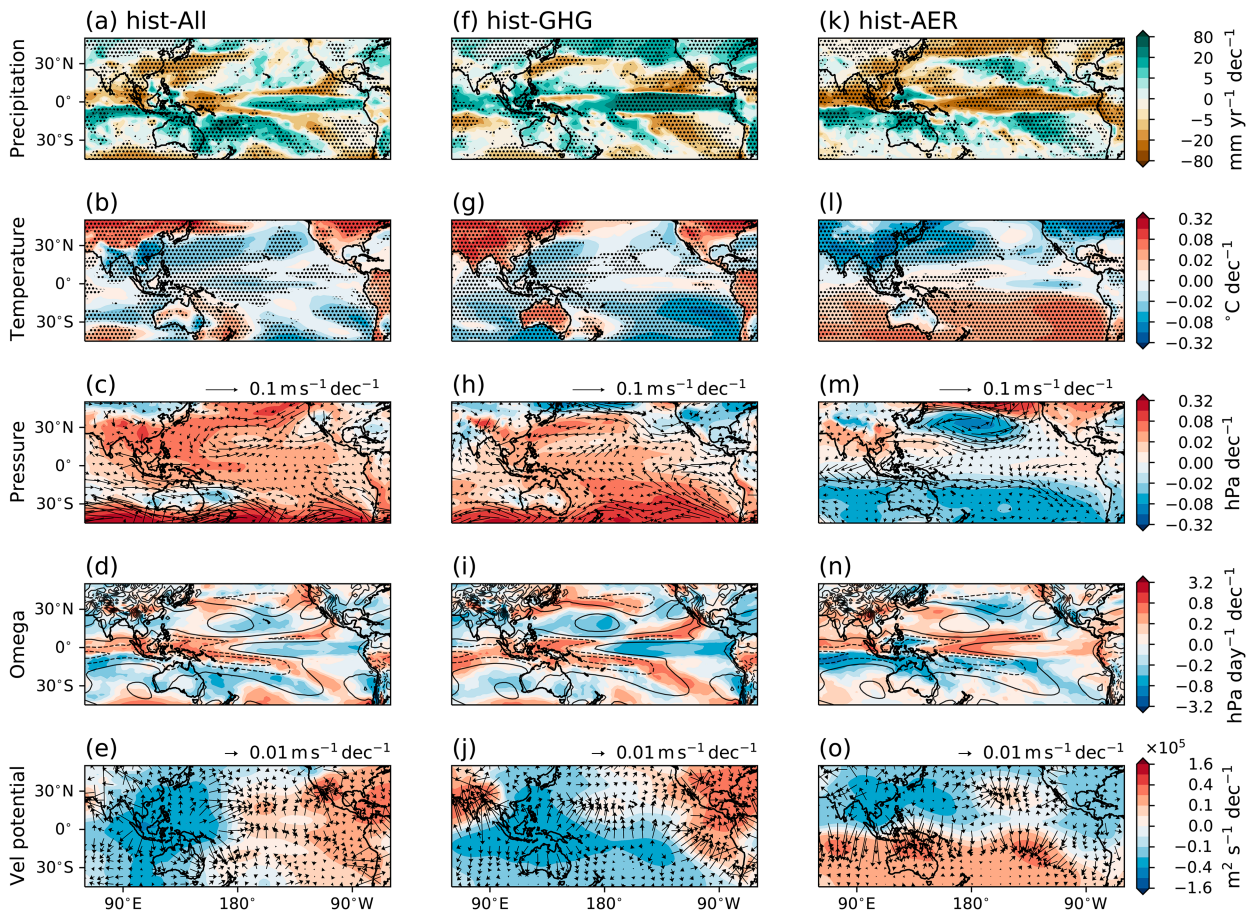


FIG. 3. Spatial distribution of trends over 1930–2014 for DJF (a),(f),(k) precipitation, (b),(g),(l) near-surface temperature after removing the tropical mean trend ( $25^{\circ}\text{N}$ – $25^{\circ}\text{S}$ ), (c),(h),(m) mean sea level pressure (colors) with 850-hPa winds (vectors), (d),(i),(n) omega at 500 hPa (colors; positive values indicate descent), and (e),(j),(o) velocity potential (colors) with divergent wind (arrows) at 850 hPa for the (left) hist-All, (center) hist-GHG, and (right) hist-AER simulations. All trends are based on the MEM across 11 CMIP6 models. Stippling indicates regions where at least 70% of the models agree on the sign of change. In (d), (i), and (n), climatological values are shown as black contours (drawn every  $30 \text{ hPa day}^{-1}$ ) with solid (dashed) contours indicating positive (negative) values.

anomalies (Fig. 3b). Over the Indo-Pacific region, an equatorial drying and wetting to the south of it indicate a southward precipitation shift (Fig. 4a) which is dynamically caused (Fig. 5c). The moisture budget analysis reveals that the  $\Delta(P - E)$  changes over NA are related to a thermodynamically and dynamically induced wetting partially compensated by a transient eddy-induced drying (Fig. 5e). The dynamic contribution is related to a relative surface cooling over India and eastern China (Fig. 3b), which leads to a strengthening of the Siberian high over this region (as also seen in reanalysis in Fig. 2b) and, in turn, a southward shift and strengthening of the monsoonal westerlies over the Indian Ocean (Fig. 3c). The anomalous cyclone off its west coast further channels this flow toward Australia, similar to the observed pattern (Fig. 2b).

The hist-GHG MEM displays positive precipitation and 850-hPa vertical velocity trends over the equatorial central-eastern Pacific Ocean similar to those in hist-All (Figs. 3a,d,f,i). In particular, an equatorward intensification and meridional narrowing of the ITCZ is evident (Figs. 3f and 4b). The large

$\Delta\text{MCD}$  term over the equatorial Pacific (Fig. 5) indicates that the ITCZ change is related to a weakening of the Indo-Pacific Walker cell (Fig. 3i) and associated El Niño-like SST pattern (Fig. 3g). However, the equatorial wetting extends farther westward across the Maritime Continent and the Indian Ocean (Fig. 3f), which appears inconsistent with the pattern of near-surface divergent flow (Fig. 3j) and 500-hPa vertical velocity (Fig. 3i). In fact, given the approximate balance in the tropics between diabatic heating and vertical velocity anomalies, one would expect excess precipitation to be distinctively associated with lower-tropospheric convergence and divergent outflow aloft. The mismatch evident from Fig. 3j and the large  $\Delta\text{TH}$  contribution to  $\Delta(P - E)$  (Figs. 5g,h) indicates a thermodynamic origin of the wetting over the Maritime Continent. This follows from a GHG-induced increase in temperature and the associated moistening, which causes an intensification of the existing patterns of moisture convergence and divergence (the “wet-gets-wetter, dry-gets-drier” paradigm; Held and Soden 2006), despite a weakening of the atmospheric circulation (Held and Soden 2006; Seager



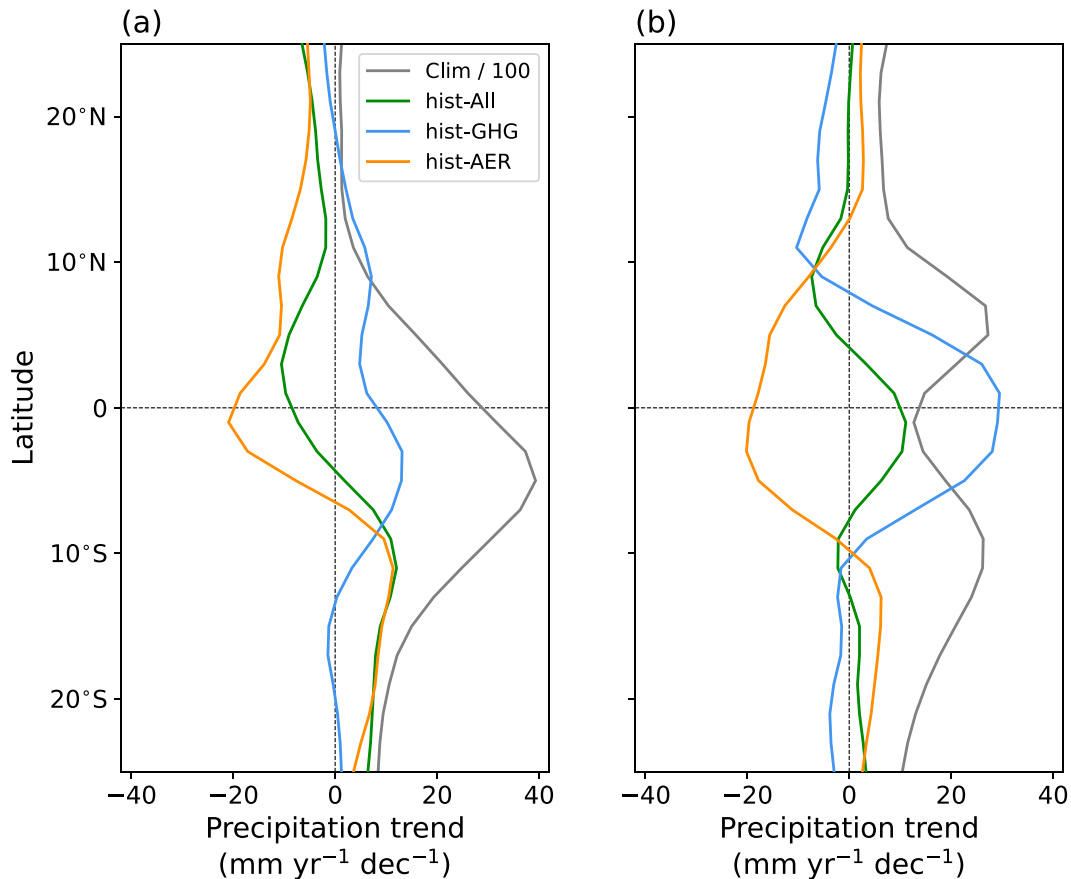


FIG. 4. Zonal-mean profile of precipitation trends across the tropical ( $25^{\circ}\text{N}$ – $25^{\circ}\text{S}$ ) (a) Indo-Pacific sector ( $70^{\circ}\text{E}$ – $180^{\circ}$ ) and (b) eastern Pacific Ocean ( $180^{\circ}$ – $70^{\circ}\text{W}$ ) for hist-All, hist-GHG, and hist-AER simulations across 11 CMIP6 models. The climatological zonal-mean profile (in units of  $\text{mm yr}^{-1}$  and divided by 100) is given for reference.

and Naik 2012). In the meridional direction, the Hadley overturning circulation over the Indo-Pacific region expands poleward and weakens (Fig. 3i) as seen by drying centered around  $35^{\circ}\text{S}$  in the  $\Delta\text{MCD}$  term (Fig. 5h), consistent with the expected response under global warming (Xian et al. 2021). The trends in the monsoonal flow and precipitation (MEM value of  $5.2 \text{ mm yr}^{-1} \text{ decade}^{-1}$ ) over NA are weak and not consistent across models (Figs. 3f,h), related largely to a compensation of the thermodynamic-induced wettening and transient eddy-driven drying (Fig. 5j).

The broad-scale features of the aerosol-induced (hist-AER) precipitation trend resemble those in the hist-GHG ensemble but with opposite sign (Figs. 3f,k). A strong meridional precipitation dipole is evident over the Indian Ocean and Maritime Continent, and is embedded in a hemispheric-wide southward shift of the ITCZ (as also seen in the zonal-mean profile in Fig. 4). This ITCZ shift is predominantly dynamically forced as seen by the large agreement between  $\Delta(P - E)$  and  $\Delta\text{MCD}$ , alongside small values of  $\Delta\text{TH}$  and  $\Delta\text{TE}$  (Figs. 5k–n): Aerosols induce a relative cooling of the NH compared to the SH during the period examined (Fig. 3l), leading to an anomalous interhemispheric southward temperature gradient and associated southward shift of the Hadley circulation to compensate for

the interhemispheric energy imbalance. The northward cross-equatorial energy flow is in the form of dry static energy and occurs in the upper troposphere associated with the northward branch of the Hadley cell (e.g., Hwang et al. 2013). At the same time, the lower branch of the Hadley cell shifts moisture (and the tropical rain belt) in the lower troposphere farther south toward NA latitudes (Figs. 3k,o). Anthropogenic aerosols further influence AUSM rainfall via regional-scale atmospheric circulation changes. Aerosols induce sea level pressure and near-surface temperature gradients across the Indian Ocean (Figs. 3l,m), which result in a strengthening and southward shift of the monsoonal westerlies. These monsoonal circulation changes, in turn, enhance the moisture convergence over NA (Figs. 5m,o), strengthen the ascending motion (Fig. 3n) and result in a wettening trend of  $9.4 \text{ mm yr}^{-1} \text{ decade}^{-1}$  over NA. This wettening is consistently simulated by the CMIP6 models and in agreement with the hist-All response (Figs. 3a,k). The temperature change over the eastern equatorial Pacific shows a La Niña-like response (Fig. 3l), consistent with a strengthening of the Indo-Pacific Walker circulation seen in the 500-hPa vertical velocity trends (Fig. 3n), which shows ascent and descent over the Maritime Continent and eastern equatorial Pacific, respectively.

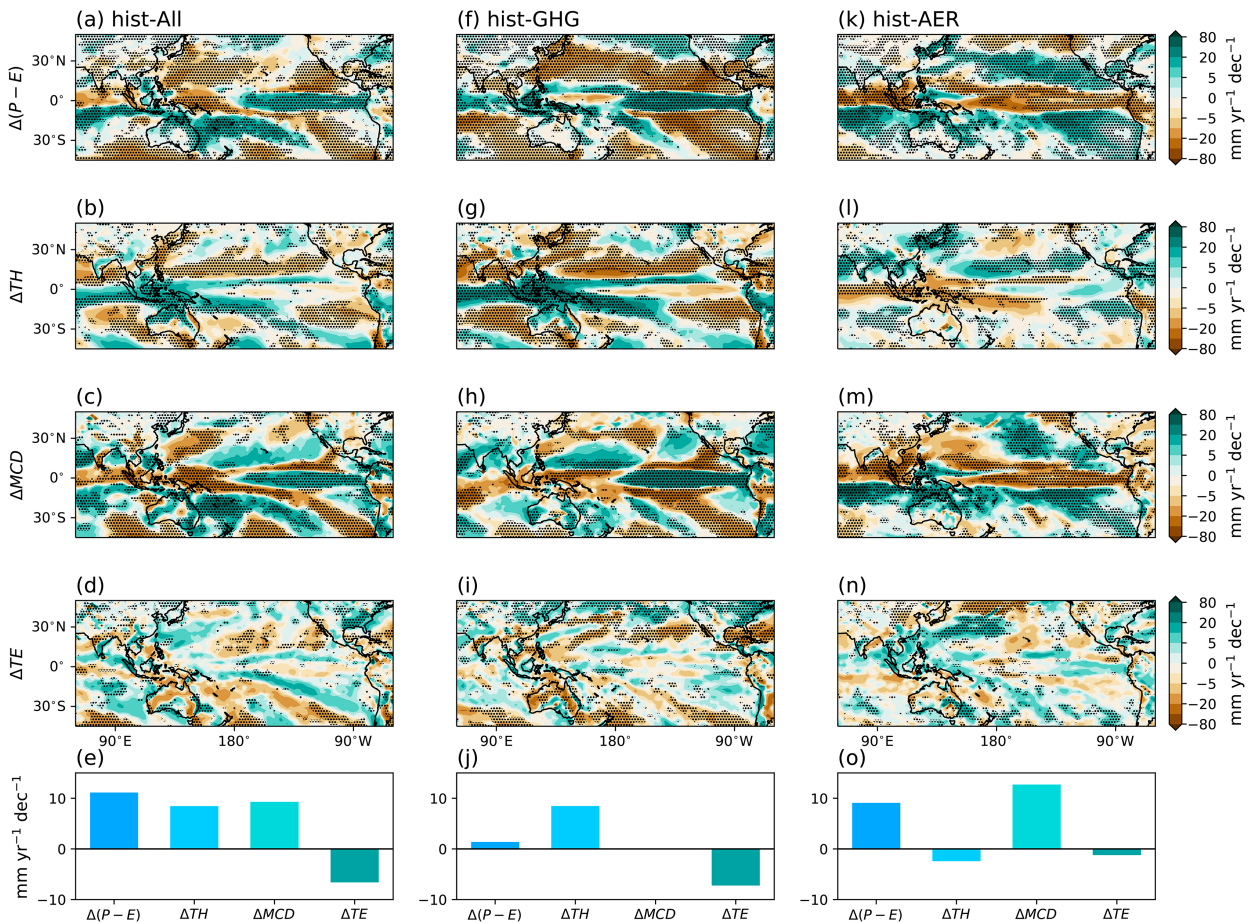


FIG. 5. Spatial distribution of trends over 1930–2014 for DJF (a),(f),(k) precipitation  $P$  minus evaporation  $E$ , (b),(g),(l) thermodynamic component  $\Delta TH$ , (c),(h),(m) mean circulation dynamic component  $\Delta MCD$ , and (d),(i),(n) transient-eddy component  $\Delta TE$  of the moisture budget decomposition for the (left) hist-All, (center) hist-GHG, and (right) hist-AER simulations. All trends are based on the MEM across 10 CMIP6 models (excluding CESM2 since it did not provide all the relevant data). Stippling indicates regions where at least 70% of the models agree on the sign of change. (e),(j),(o) The contributions of the different moisture budget terms over NA.

Some previous studies have shown that interactions between anthropogenic aerosols and GHGs can result in an SH climate response that differs from the linear combination of their individual effects (e.g., Ming and Ramaswamy 2009), while others found small nonlinearities over Australia (e.g., Shiogama et al. 2013). Figures 3 and 4 show that the hist-All response is, to a very good approximation, the result of the linear combination of the individual anthropogenic aerosol and GHG responses over the tropics. Interestingly, we also find a “tropical Pacific east–west divide” with aerosol forcing dominating the all-forcing response over the tropical Indo-Pacific sector, including NA, and GHG forcing over the tropical eastern Pacific (approximately east of the date line) (Figs. 3 and 5). This finding is further confirmed by analyzing the spatial correlation values of precipitation: Over the Indo-Pacific sector ( $25^{\circ}\text{S}$ – $25^{\circ}\text{N}$ ,  $70^{\circ}\text{E}$ – $180^{\circ}$ ), the spatial correlation of precipitation between hist-All and hist-AER is 0.65, while the correlation with hist-GHG is only 0.07. Over the tropical eastern Pacific Ocean ( $25^{\circ}\text{S}$ – $25^{\circ}\text{N}$ ,  $180^{\circ}$ – $70^{\circ}\text{W}$ ; note that the Pacific and Indo-Pacific boxes chosen are of the same size), the spatial

correlation between hist-All and hist-GHG is 0.56, but  $-0.18$  for hist-AER.

The large agreement between the precipitation and circulation trends in hist-All and hist-AER as well as the large aerosol-induced  $\Delta MCD$  contribution to  $\Delta(P - E)$  over the Indo-Pacific sector (Figs. 3 and 5) indicates that anthropogenic aerosols have significantly influenced the Indo-Pacific climate and played a dominant role in the wetting trend over NA by inducing a southward shift and strengthening of the monsoonal westerlies (Figs. 3 and 4a). GHGs have played a minor role in determining these changes across the Indo-Pacific sector and NA as the precipitation pattern and trends in other climate variables do not show large agreement (Fig. 3). Nonetheless, it should be noted that the moisture budget decomposition shows not only an aerosol-induced dynamic contribution to the precipitation changes over NA (Fig. 5). GHGs induce a strong thermodynamic precipitation increase over the Maritime Continent, extending toward NA (Fig. 5g). However, this GHG-induced wetting seems to be largely compensated by the GHG-induced drying through transient eddy changes (Fig. 5i). This leads to no large-scale

changes in  $\Delta(P - E)$  over NA in the hist-GHG simulations (Fig. 5j) and favors the dominance of the dynamic precipitation changes due to aerosols over NA in the hist-All simulations (Fig. 5e). The large-scale agreement of  $P$  and  $\Delta(P - E)$  between the hist-All and hist-AER response but low agreement with hist-GHG (Figs. 3 and 5) provides further support to anthropogenic aerosols being the dominant drivers of the precipitation response over NA.

This hypothesis is additionally corroborated by the analysis of the CESM2 Large Ensemble simulations, which similarly show a strengthening and southward shift of the monsoonal westerlies and subsequent precipitation increase over NA due to aerosol forcing (Fig. A1). A detailed description of the CESM2 Large Ensemble analysis can be found in the appendix. This aerosol-induced wettening is largely independent of the sign of Atlantic meridional overturning circulation (AMOC) (Fig. S3 with description) anomalies, highlighting the negligible influence of this mode of variability on the historical AUSM rainfall trend.

## 2) INTERMODEL DIFFERENCES IN SIMULATED TRENDS

We further examined the intermodel spread in AUSM rainfall trends simulated by the 11 CMIP6 models. For this, we calculated the mean for each model across the first three realizations (i.e., the maximum number of members common to all models) to give equal weight to each model and show the spread in the response (Fig. 6). All models except for BCC-CSM2-MR show an increasing precipitation trend in their hist-All mean, although the magnitude of the observed trend (the black solid line in Fig. 6) is consistently underestimated by all models. The GHG-induced precipitation response reveals a large intermodel spread in the sign of the response with no overall consensus (five models simulate a positive trend, four a negative trend, and two a near-zero mean trend). The low model agreement regarding the sign of the precipitation trend over NA indicates large uncertainties around the processes underpinning the GHG-related precipitation response over NA. In particular, the dynamically induced precipitation changes over NA contribute to this uncertainty as seen by the low model agreement regarding the sign of change in  $\Delta\text{MCD}$  over NA (Fig. 5g). In contrast, 9 out of the 11 hist-AER ensemble means show an increasing precipitation trend. Three models (ACCESS-CM2, CESM2, and NorESM2-LM) simulate a particularly strong wettening over NA, above the 95th percentile of the respective PDF distribution. Nonetheless, the spread in the simulated magnitude of the precipitation trend over NA in response to the aerosol forcing is large, likely related to the influence of internal variability and structural model differences.

While a detailed analysis of these causes of model diversity is beyond the scope of our study, we performed a preliminary analysis to investigate a potential link between aerosol radiative forcing values or historical/climatological model biases with the simulated AUSM trends across the various models. For the former, we find that models with less (more) negative effective radiative forcing due to shortwave aerosol–radiation (aerosol–cloud) interactions simulate more realistic AUSM trends in hist-AER (statistically significant correlation of 0.63

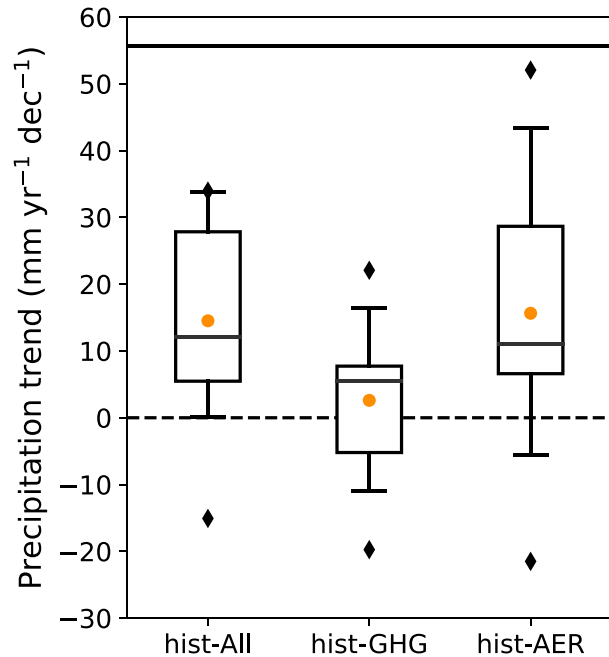


FIG. 6. Boxplot of the DJF 1930–2014 trends in precipitation over Northern Australia ( $10^{\circ}$ – $20^{\circ}$ S,  $120^{\circ}$ – $150^{\circ}$ E; land only) in the hist-All, hist-GHG, and hist-AER simulations. The ensemble mean across the first three realizations for each of the 11 CMIP6 models is used as input data to give equal weight to each model. The boxes show the first and third quartiles with whiskers extending to the 5th–95th percentiles. The diamonds represent outliers, and the orange circle represents the mean values. The black solid line represents the observed precipitation trend of  $55.7 \text{ mm yr}^{-1} \text{ decade}^{-1}$  based on GPCC data.

and  $-0.69$ , respectively; see Fig. S4). For the latter, one should note that the accuracy of attributing simulated regional climate change to human influence is closely tied to the model's ability to replicate the baseline climatic conditions (e.g., Matsueda and Palmer 2011). Previous studies have demonstrated a relationship between model biases and the associated climate response, for instance, for tropical circulation (Zhou and Xie 2015) and rainfall (Chadwick et al. 2016). We, thus, investigated differences in the historical trends and climatological biases for 30 different CMIP6 models, which we divided into DRY or WET groups based on the sign of the simulated hist-All AUSM rainfall trend (see supplemental material section 7 for more detail). We find that the ability of models to reproduce the increasing AUSM rainfall trend might be linked to an aerosol signal projecting onto stronger monsoonal westerly winds and an already further southward-located ITCZ in the WET compared to the DRY climatology, which in turn results in a stronger historical precipitation increase over NA (Fig. S6). In contrast, we find no link between the magnitude of the cold tongue bias, global mean warming trend, or equilibrium climate sensitivity of the individual CMIP6 models and the simulated strength or sign of the precipitation trend over NA (Fig. S7). Future research could further investigate the factors influencing the intermodel spread



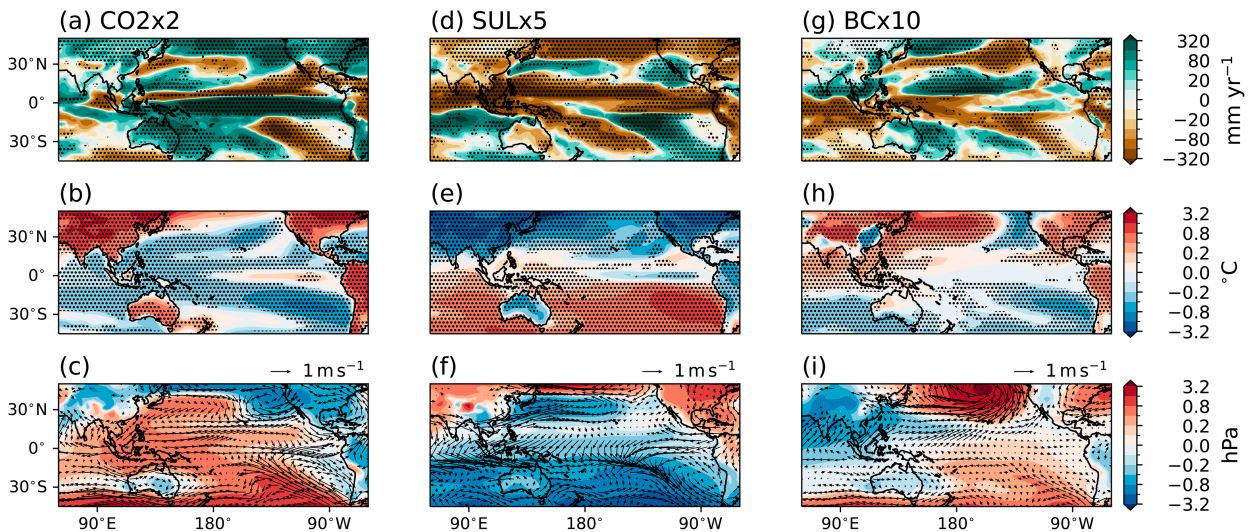


FIG. 7. Spatial anomalies during austral summer in (a),(d),(g) precipitation, (b),(e),(h) near-surface temperature after removing the tropical mean ( $25^{\circ}\text{N}$ – $25^{\circ}\text{S}$ ), and (c),(f),(i) mean sea level pressure (color) with 850-hPa winds (vectors) for the total equilibrium response in the (left)  $\text{CO}_2 \times 2$ , (center)  $\text{SUL} \times 5$ , and (right)  $\text{BC} \times 10$  simulations from PDRMIP. Nine models were used to calculate the multimodel mean, and stippling indicates regions where at least 80% of the models agree on the sign of change.

in simulated precipitation trends over NA by focusing, for instance, on the role of differences between the aerosol representations across the models.

### 3) ATTRIBUTION OF DRIVERS USING PDRMIP

We used global ( $\text{CO}_2 \times 2$ ,  $\text{SUL} \times 5$ , and  $\text{BC} \times 10$  in Fig. 7) and regional ( $\text{SUL} \times 10\text{Asia}$ ,  $\text{SUL} \times 10\text{Eur}$ , and  $\text{BC} \times 10\text{Asia}$  in Fig. 8) experiments from PDRMIP to further examine the influence of anthropogenic aerosols on AUSM rainfall and, in

particular, facilitate the identification of the dominant aerosol source region. Increased  $\text{CO}_2$  leads to a contraction and strengthening of the ITCZ (Fig. 7a), which is dominated by slow climate adjustments (Figs. S8a,b). This is related to a weakening of the Indo-Pacific Walker cell, ensuing weakening of the equatorial trade winds and an emerging El Niño-like SST pattern (Figs. 7b,c). Over the Indo-Pacific sector, the  $\text{CO}_2$  increase induces anomalous equatorial easterlies (Fig. 7c) and no clear precipitation dipole, both of which are in contrast to the pattern in the hist-All ensemble (Figs. 3a,c). Interestingly,

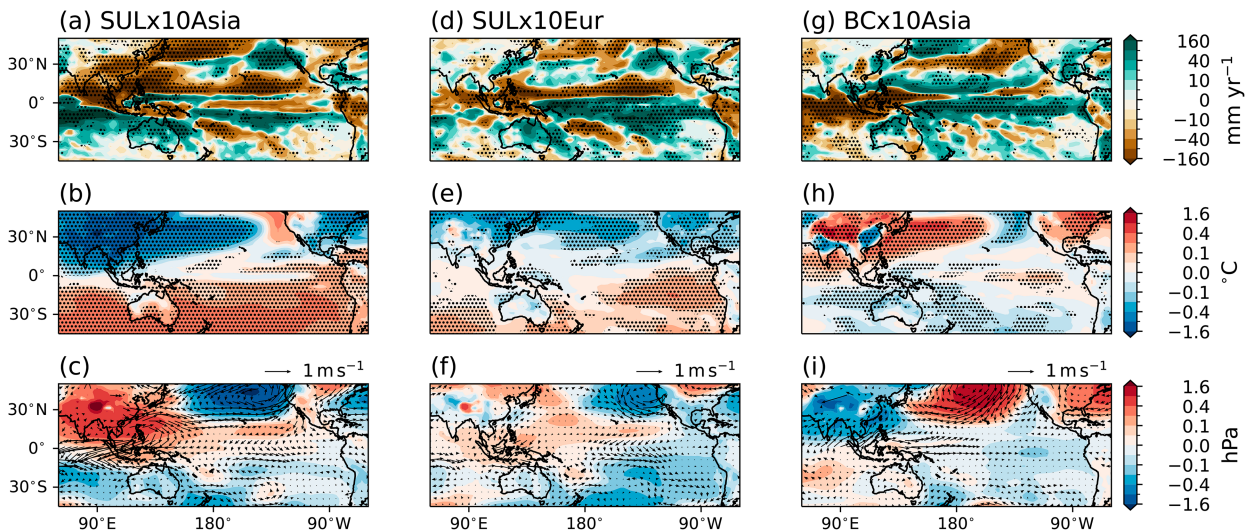


FIG. 8. Spatial anomalies during austral summer in (a),(d),(g) precipitation, (b),(e),(h) near-surface temperature after removing the tropical mean ( $25^{\circ}\text{N}$ – $25^{\circ}\text{S}$ ), and (c),(f),(i) mean sea level pressure (color) with 850-hPa winds (vectors) for the total equilibrium response in the (left)  $\text{SUL} \times 10\text{Asia}$ , (center)  $\text{SUL} \times 10\text{Eur}$ , and (right)  $\text{BC} \times 10\text{Asia}$  simulations from PDRMIP. Six models were used to calculate the multimodel mean, and stippling indicates regions where at least 80% of the models agree on the sign of change. Note that the values are halved in comparison to Fig. 7.



a large fast precipitation increase over Australia, although with a large intermodel spread in the magnitude (Fig. S10), is evident while all other regions are controlled by ocean-mediated changes (Fig. 7a, Figs. S8a,b). This NA wettening is likely linked to a strong thermodynamic control from land and atmospheric warming on precipitation in response to the extensive step increase in CO<sub>2</sub> (considering the exponential Clausius–Clapeyron scaling), which dominates over the slow adjustments (Figs. S8a,b). This thermodynamic response is similar to the ΔTH changes seen in the hist-GHG simulations (Fig. 5f) but, other than in hist-GHG, does not seem to be compensated by changes in ΔTE (Figs. 3f and 5e–h).

The SUL×5 simulations show a southward displacement of the mean position of the ITCZ due to the aerosol-induced interhemispheric temperature gradient (Figs. 7d,e). That a significant strengthening, but no shift, of the monsoonal flow occurs over the Indo-Pacific sector is evident (Fig. 7f). The NA rainfall response shows a minimal decrease, with poor consistency across models (Fig. S10), in contrast to the hist-All simulations (Fig. 3a). Overall, precipitation changes over NA show nearly the opposite pattern on fast and slow time scales with drying and wettening, respectively (Figs. S8c,d).

The climate response to Asian sulfate aerosol emissions (SUL×10Asia) shows large agreement with the hist-All and hist-AER trends (Figs. 3 and 8a–c). In particular, Asian sulfate aerosols induce a strong cross-hemispheric temperature gradient and a southward shift and strengthening of the monsoonal westerlies (Figs. 8b,c). The associated precipitation dipole over the Indian Ocean and precipitation increase over NA is simulated by most PDRMIP models (Fig. 8a, Fig. S10) and in agreement with the pattern shown by the hist-All simulations (Fig. 3a). The precipitation anomaly over NA is largely controlled by atmospheric adjustments over the northeastern part and oceanic adjustments over the northwestern part (Figs. S9a,b). Over the equatorial Pacific, the precipitation changes suggest a small southward shift of the ITCZ (Fig. 8a).

The most pronounced precipitation changes associated with variations in European sulfate aerosols (SUL×10Eur) occur over the tropical Pacific, which feature a large-scale strengthening of the ITCZ and drying north of the equator (Fig. 8d) due to oceanic adjustments (Figs. S9c,d). Besides, a drying over the northern Indian Ocean and a small precipitation increase over NA are shown, although these responses are inconsistent across models (Fig. S10) and not related to clear changes in the monsoonal flow (Figs. 8d,f). Thus, these climate anomalies do not strongly resemble the hist-All response, although they might have strengthened the AUSM precipitation trend to Asian sulfate aerosols minimally (Figs. 3a–c).

Global (BC×10) and Asian (BC×10Asia) black carbon emissions lead to a precipitation decrease over the equatorial Indian Ocean and wettening over the northern Indian Ocean (Figs. 7g and 8g), in contrast to the hist-All simulations (Fig. 3a). The precipitation increase over NA is dominated by atmospheric adjustments (Figs. S8e–f and S9e–f), although there is a large spread in the model responses and no model agreement on the sign of change in BC×10 (Fig. S10). Besides, the increase in black carbon induces mean sea level pressure and temperature

gradients (Figs. 7h,i and 8h,i) which are nearly opposite to the patterns seen in hist-All (Figs. 3b,c).

#### 4. Discussion and conclusions

This study aimed to identify drivers and physical mechanisms associated with the long-term increase in Australian summer monsoon rainfall between 1930 and 2014, a topic that remains debated (Heidemann et al. 2023).

Our analysis shows that the observed increase in AUSM rainfall lies at the upper range (i.e., above the 95th percentile) of the internal variability distribution derived from the preindustrial control simulations from 11 CMIP6 models (Fig. 1d). This finding extends previous research which identified the existence of an anthropogenically forced component in the NWA precipitation trend since the 1950s (Rotstayn et al. 2012; Frederiksen and Grainger 2015; Knutson and Zeng 2018).

To isolate the effect of anthropogenic drivers on the AUSM rainfall trend, we used historical all- and single-forcing simulations from a suite of CMIP6 models and the CESM2 Large Ensemble. A comprehensive summary of our results is provided in Table S3. We find that anthropogenic aerosol emissions played a dominant role in driving precipitation trends over the Indo-Pacific sector, including NA, while the response to increased greenhouse gas concentrations prevailed over the wider tropical Pacific region (Figs. 3 and A1). We termed this spatial division between the area of impact of anthropogenic aerosols and GHGs on precipitation over the Pacific region the “tropical Pacific east–west divide.” The comparison with idealized PDRMIP simulations revealed that sulfate emissions over Asia, predominately eastern China, led to a strengthening and southward shift of the monsoonal westerlies and ensuing increase in AUSM rainfall (Figs. 8a–c; see also Table S3). In contrast, the influence of European sulfate and Asian black carbon aerosols on NA precipitation was found to be negligible (Figs. 8d–i; see also Table S3). This attribution is consistent with historical aerosol emission changes between 1930 and 2014. Specifically, sulfate aerosol emissions from Europe and the United States experienced a significant increase during the mid-twentieth century, followed by a decline below 1930 levels by 2014 (e.g., Hoesly et al. 2018). In contrast, sulfate emissions from Asia have rapidly and monotonically increased since the 1930s, exceeding the emission levels of Europe and the United States since the 1990s (e.g., Myhre et al. 2017a).

We further investigated the physical mechanism linking forcing and response as summarized in Fig. 9. The climatological circulation pattern is characterized by the zonal Indo-Pacific Walker cell and the local meridional Hadley cell (Fig. 9a). The ascending motion over the Maritime Continent leads to strong convection and precipitation, while the inflow of moist air from the northwest brings monsoonal rainfall to NA during austral summer (Drosowsky 1996). However, anthropogenic forcing has significantly modulated this pattern since the early twentieth century (Figs. 8b–d).

We found that the impact of GHGs was predominantly evident over the equatorial region (Fig. 9b). The precipitation increase over the Maritime Continent and the equatorial

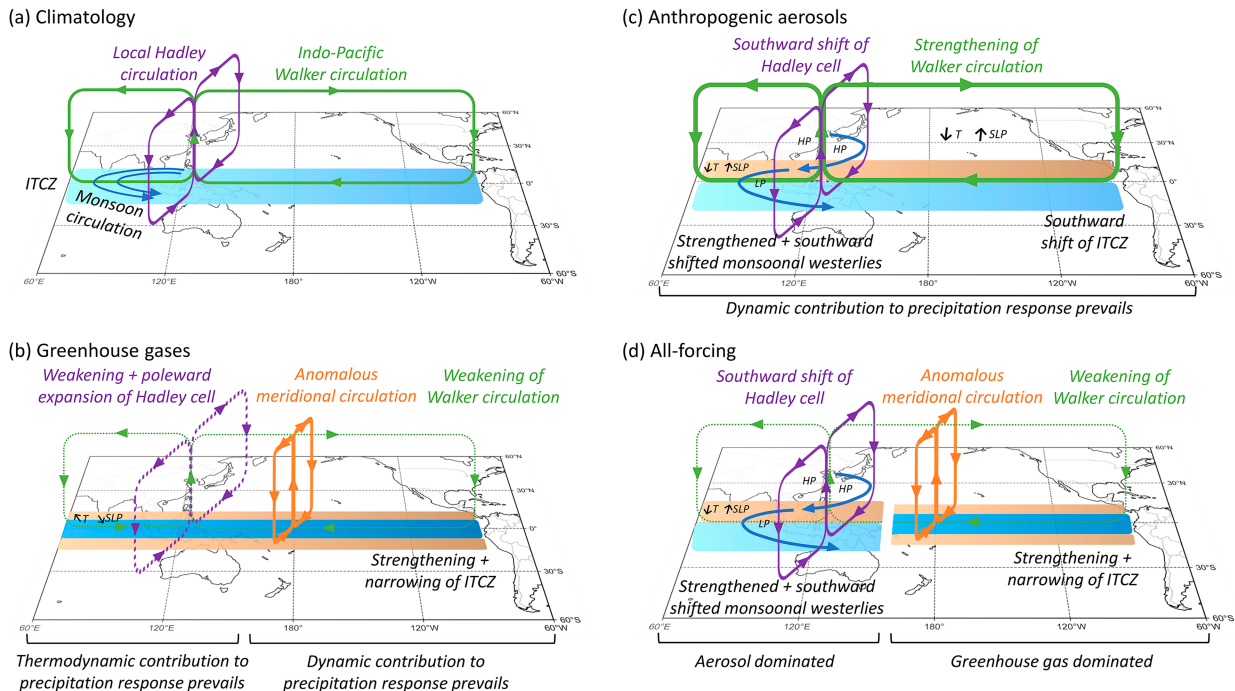


FIG. 9. Schematic of the large-scale circulation adjustments during austral summer (DJF) between 1930 and 2014 caused by (b) greenhouse gases, (c) anthropogenic aerosols, and (d) all forcings combined. (a) A conceptual representation of the climatological circulation during austral summer for reference. The local meridional Hadley circulation and zonal Indo-Pacific Walker circulation are shown by purple and green arrows, respectively. Strengthened circulation cells are drawn with thicker lines and weakened cells with dashed lines. Precipitation increase and decrease are shown by shaded areas in blue and brown, respectively, and ITCZ refers to the intertropical convergence zone. Marked gradients in temperature ( $T$ ) and sea level pressure (SLP) are indicated by arrows pointing in the direction of increasing values. High and low pressure trends are denoted by HP and LP, respectively.

Indian Ocean is of thermodynamic origin due to the GHG-induced increase in atmospheric water vapor according to the Clausius–Clapeyron scaling and intensification of the hydrological cycle in agreement with results from Held and Soden (2006) and Seager and Naik (2012). However, this thermodynamic precipitation increase over NA was largely compensated by the transient eddy-induced drying, resulting in modest precipitation changes over NA with no model agreement regarding the sign of change (five models simulate a positive trend, four a negative trend, and two a near-zero mean trend). Over the Pacific Ocean, observed and simulated hist-All precipitation patterns were largely controlled by GHG-induced dynamic changes through weakening of the Indo-Pacific Walker circulation to satisfy the global energy constraints (Held and Soden 2006; Vecchi and Soden 2007; O’Gorman et al. 2012). This led to an El Niño-like response with a weakening of the equatorial Pacific easterlies (as inferred from the 925-hPa winds; not shown), relative warming of the eastern equatorial SSTs, and subsequent ascending trend leading to a precipitation increase over the ITCZ core region. This ITCZ strengthening was of dynamic origin (i.e., due to circulation adjustments caused by nonthermodynamic drivers) similar to Seager et al. (2010) and induced a strong anomalous meridional circulation with associated precipitation decrease north and south of the equator (i.e., ITCZ narrowing). This off-equatorial drying was further strengthened

by thermodynamic adjustments. Additionally, GHGs lead to a poleward expansion and weakening of the Hadley circulation. These findings are consistent with observed changes in large-scale circulation adjustments under global warming (e.g., Vecchi and Soden 2007; Vecchi et al. 2006; Xian et al. 2021) and precipitation reconstruction (Ren et al. 2013) but cannot be further corroborated due to the lack of oceanic precipitation data in the presatellite era.

Our results show that the impact of both global and regional anthropogenic aerosol emissions on tropical precipitation was primarily linked to dynamical adjustments, with strong circulation anomalies in the meridional direction but modest ones in the zonal direction (Fig. 9c). Sulfate aerosol emissions over East Asia had the largest impact on NA precipitation causing a higher aerosol burden over this region, reduction in surface downwelling shortwave radiation, and subsequent near-surface air cooling trend. Thermodynamic circulation adjustments to this cooling led to a strengthening of the southeastern edge of the Siberian high over eastern China and the East China Sea, which intensified the East Asian winter monsoon circulation and extended it southeastward. The compensating low pressure anomaly over the Maritime Continent, together with the aerosol-induced meridional gradient in the temperature trend across the northern to central Indian Ocean (Fig. 3f), led to a strengthening and southward shift of the AUSM climatological westerlies and ensuing

dynamic precipitation increase over NA (although with large model spread of the simulated magnitude of this trend). This manifested in a southward shift of the local Hadley cell, in agreement with results from Liu et al. (2019). Our preliminary analysis of atmosphere-only simulations with prescribed SSTs further supports the important role of dynamical adjustments and atmosphere–ocean interactions on NA precipitation through changes in SSTs and associated monsoonal circulation trends (see supplemental material section S12 for more details). Overall, these local changes were embedded in an aerosol-induced interhemispheric temperature gradient which led to a shift of the ITCZ to the warmer hemisphere (i.e., SH). The southward shift in the tropical rain belt occurs in conjunction with a northward cross-hemispheric flow of dry static energy in the upper troposphere, as a circulation response to restore the interhemispheric energy imbalance caused by anthropogenic aerosols (Hwang et al. 2013). Previous studies (e.g., Ming and Ramaswamy 2009; Allen and Sherwood 2011) have similarly found a robust southward shift of the ITCZ in response to a stronger aerosol-induced cooling of the NH. We further find that anthropogenic aerosol emissions led to a modest strengthening of the Walker circulation with strengthened ascent and descent located over the Maritime Continent and off the west coast of South America, respectively.

The full historical (i.e., hist-All) response over NA shows that the dynamically induced precipitation changes due to aerosols play a key role in contrast to the compensating thermodynamically induced wettening and transient eddy-related drying due to GHGs (Fig. 5e). At a large scale, the all-forcing response can be seen as a spatial combination of aerosol- and GHG-induced adjustments with the former dominating over the Indo-Pacific sector, including NA, and the latter over the wider Pacific Ocean approximately east of the date line (and the zonal direction) (Figs. 9b–d). This tropical Pacific east–west divide can be understood by considering that anthropogenic aerosols, due to their spatially heterogeneous distribution, are more effective than well-mixed GHGs in leading to regional dynamical changes, especially in the meridional direction, as the atmospheric–oceanic system adjusts to compensate for the energy imbalance between the emission region and the surroundings. Note, for instance, the strong monsoonal westerly trend in the hist-AER simulations and associated precipitation trend over the Indo-Pacific (Figs. 3k,m), which are roughly an order of magnitude larger than those in response to GHGs (Figs. 3f,h). In contrast, the GHG-induced Indo-Pacific Walker cell changes and linked precipitation adjustments dominate over the aerosol-induced changes in hist-All (Fig. 3). Similarly, Bollasina et al. (2011) concluded that GHG-induced warming dominated the zonal circulation response while anthropogenic aerosol effects prevailed in the meridional direction in the late twentieth century, although their study focused on June–September. Nonetheless, previous studies have found a similar global-scale climate pattern in response to greenhouse gas and aerosol emissions but of opposite sign (Xie et al. 2013; Persad et al. 2018; Cao et al. 2022b), although these studies focused on global rather than regional-scale climate responses.

Our conclusion that Asian anthropogenic aerosols played a key role in the twentieth-century precipitation increase over NA agrees with previous results from studies using single-model (Rotstayn et al. 2007, 2012) and multimodel approaches (Dey et al. 2019). However, their conclusions were limited by a simplified treatment of aerosol processes (Rotstayn et al. 2007, 2012), a strong cold tongue model bias of the analyzed model (Rotstayn et al. 2007, 2012; Shi et al. 2008; Cai et al. 2011), uncertainties regarding the underlying physical mechanism (Rotstayn et al. 2012; Dey et al. 2019), and lack of model agreement with observations (Rotstayn et al. 2007, 2012; Dey et al. 2019). Additionally, the study by Dey et al. (2019) compared the mean climate response across 18 CMIP5 models for the hist-All simulations to the mean across nine CMIP5 models with a different number of ensemble members for the hist-AER simulations, hindering an adequate attribution of the NWA precipitation trend. Our current study addresses these limitations while further offering a detailed mechanistic analysis as well as a multimodel comparison of the climate responses to different aerosol types and emission regions. We also provide a more robust assessment of observed long-term trends in AUSM precipitation (Fig. 1) which suggests that our conclusions are independent of the exact period analyzed—despite the large influence of decadal to multidecadal variability in AUSM rainfall (Power et al. 1999)—with longer (e.g., 1920–2014) or shorter (e.g., 1940–2014) trends showing similar climate adjustments (not shown).

We acknowledge that there are some potential limitations to this study. First, the magnitude of the AUSM rainfall trend is underestimated by the MEM across 11 CMIP6 models, although most models capture the sign of the trend (Fig. 6). Since some realizations from the suite of CMIP6 models and the CESM2 Large Ensemble accurately reproduce the magnitude (not shown), our analysis suggest that the observed trend likely results from a combination of aerosol-forced changes and internal variability. In particular, variability of the SST gradient between the Indo-Pacific and eastern Pacific has been found to influence historical SH monsoonal trends (Cao et al. 2023). Second, the signal-to-noise ratio (computed as the ratio of the precipitation change divided by the interannual standard deviation) for the observed AUSM precipitation trend from 1930 to 2014 is approximately 0.9. While this indicates comparable magnitudes of signal and noise on multidecadal time scales, the noise intermittently exceeded the trend on interannual time scales (see also Fig. 1b). Third, while we find that the climate response can be largely attributed to the effect of Asian sulfate aerosols, other forcing agents (such as GHGs or black carbon aerosols) as well as internal variability might have contributed to the observed AUSM rainfall trend. We find a large intermodel spread in the GHG-induced sign of AUSM precipitation change which translates into a corresponding large uncertainty on the role of GHGs and hinders further quantitative assessment. Additionally, while the MEM is able to reproduce the broad features of the historical surface temperature response pattern, it also shows some systematic biases relative to observations. These biases introduce some additional uncertainties in the subsequent analysis. Overall, our results emphasize the need

for a better understanding of the influence of model biases, the underlying reasons for the intermodel spread, and the interplay between aerosols and internal variability on historical changes in AUSM rainfall.

Despite these limitations, our study contributes to an improved understanding of the impact of Asian anthropogenic aerosols on the historical increase in AUSM rainfall and the associated dynamical mechanism over the Indo-Pacific sector. The dependence of the AUSM response on the aerosol source region found here provides additional evidence for the importance of regional aerosol emissions in shaping global and regional climate (e.g., Wilcox et al. 2019; Persad 2023; Fahrenbach and Bollasina 2023). Further scientific advances are needed to reduce uncertainties in future projections of AUSM rainfall under different aerosol emission trajectories and to develop adaptation policies, especially given the rapidly evolving emissions over Asia (Li et al. 2017; Samset et al. 2019). This is particularly important to ensure the future productivity and profitability of NA's agricultural economy, with cattle and sugar exports alone generating over \$3 billion in annual income (CSIRO 2020). Further analysis could also focus on the influence of aerosol forcing on driving changes in the MJO as well as on potential seasonal shifts in AUSM rainfall, rather than seasonal averages only, which is a critical factor controlling agricultural production (Qureshi et al. 2013).

*Acknowledgments.* N. L. S. F., M. A. B., B. H. S., and A. M. L. E. acknowledge support from the Research Council of Norway (324182; CATHY). M. A. B. also acknowledges support from the Natural Environment Research Council (NE/N006038/1). T. C. is funded by Meat and Livestock Australia, the Queensland Government through the Drought and Climate Adaptation Program, and the University of Southern Queensland through the Northern Australia Climate Program (NACP).

*Data availability statement.* GPCC precipitation is publicly available through the Global Precipitation Climatology Centre via [https://doi.org/10.5676/DWD\\_GPCC/FD\\_M\\_V2022\\_050](https://doi.org/10.5676/DWD_GPCC/FD_M_V2022_050). CRU precipitation can be accessed through the Centre for Environmental Data Analysis (CEDA) Archive via <https://catalogue.ceda.ac.uk/uuid/e0b4e1e56c1c4460b796073a31366980>. AWAP precipitation data are available upon request from the Australian Bureau of Meteorology. HadISST SST data are available through the CEDA Archive via <https://catalogue.ceda.ac.uk/uuid/542291c0956a3e4ea2c5085f1a31b94a>.

ceda.ac.uk/uuid/542291c0956a3e4ea2c5085f1a31b94a. Twentieth Century Reanalysis data are available through the National Oceanic and Atmospheric Administration (NOAA) at [https://psl.noaa.gov/data/gridded/data.20thC\\_ReanV3.html](https://psl.noaa.gov/data/gridded/data.20thC_ReanV3.html). The CMIP6 simulations used in this study are published on the CMIP6 archive available via the Earth System Grid Federation (ESGF) at <https://esgf-node.llnl.gov/projects/esgf-llnl/>. The CESM2 Large Ensemble simulations used in this study are available at <https://www.earthsystemgrid.org/dataset/ucar.cgd.cesm2le.output.html> and <https://www.earthsystemgrid.org/dataset/ucar.cgd.cesm2.single.forcing.large.ensemble.html>. The PDRMIP data can be accessed through the World Data Center for Climate (WDCC) data server at [https://doi.org/10.26050/WDCC/PDRMIP\\_2012-2021](https://doi.org/10.26050/WDCC/PDRMIP_2012-2021).

## APPENDIX

### Precipitation and Large-Scale Climate Response in the CESM2 Large Ensemble

We investigated the impact of anthropogenic forcing agents further by examining precipitation trends and the associated large-scale climate patterns in the CESM2 Large Ensemble (Fig. A1). The CESM2-All SMBB simulations (Fig. A1a) can reproduce the observed precipitation pattern over Australia (Fig. 1c). These simulations—in agreement with results from the suite of CMIP6 models—indicate that aerosols are instrumental to explain the precipitation and wind response over the Indo-Pacific region, including Australia, while the response to GHGs shows little ensemble consensus on the sign of change (Figs. A1a,d,g). Specifically, anthropogenic aerosols lead to a hemispheric-wide temperature gradient with ensuing southward shift and strengthening of the monsoonal westerlies over the Indian Ocean (Figs. A1b,c,h,i). In contrast, the GHG-induced changes are mainly located over the equatorial Pacific with a strengthening and meridional narrowing of the ITCZ related to an El Niño-like SST pattern (Figs. A1d–f). Interestingly, the CESM2-All SMBB simulation shows a weak signal in precipitation over the equatorial eastern Pacific with little ensemble agreement, suggesting a significant influence of internal variability (Fig. A1a). Besides, biomass burning aerosols might influence this response as the CESM2-All CMIP6 simulations show a pronounced equatorial wettening (not shown).



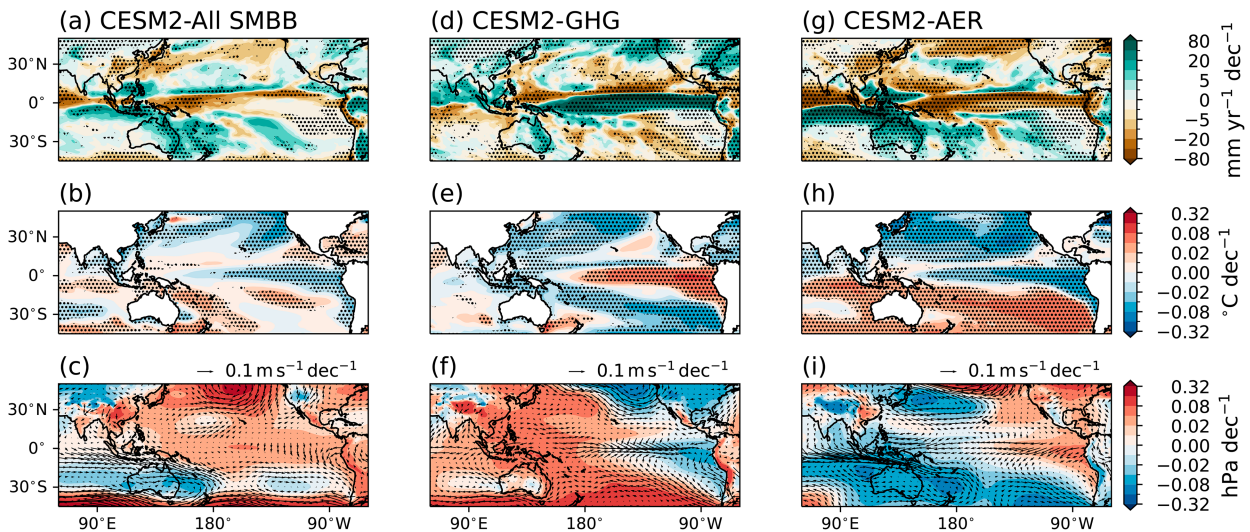


FIG. A1. Spatial distribution of trends over 1930–2014 for DJF (a),(d),(g) precipitation, (b),(e),(h) sea surface temperature after removing the tropical mean trend (25°N–25°S), and (c),(f),(i) mean sea level pressure (color) with 850-hPa winds (vectors) in the (left) CESM2-All SMBB (40 ensembles), (center) CESM2-GHG (15 ensembles), and (right) CESM2-AER (20 ensembles) simulations from CESM2 Large Ensemble. Stippling shows regions where at least 70% of the ensemble members agree on the sign of change.

## REFERENCES

- Albrecht, B. A., 1989: Aerosols, cloud microphysics, and fractional cloudiness. *Science*, **245**, 1227–1230, <https://doi.org/10.1126/science.245.4923.1227>.
- Allen, R. J., and S. C. Sherwood, 2011: The impact of natural versus anthropogenic aerosols on atmospheric circulation in the Community Atmosphere Model. *Climate Dyn.*, **36**, 1959–1978, <https://doi.org/10.1007/s00382-010-0898-8>.
- , J. R. Norris, and M. Kovilakam, 2014: Influence of anthropogenic aerosols and the Pacific decadal oscillation on tropical belt width. *Nat. Geosci.*, **7**, 270–274, <https://doi.org/10.1038/ngeo2091>.
- Biasutti, M., and A. Giannini, 2006: Robust Sahel drying in response to late 20th century forcings. *Geophys. Res. Lett.*, **33**, L11706, <https://doi.org/10.1029/2006GL026067>.
- Bollasina, M. A., Y. Ming, and V. Ramaswamy, 2011: Anthropogenic aerosols and the weakening of the South Asian summer monsoon. *Science*, **334**, 502–505, <https://doi.org/10.1126/science.1204994>.
- Borowiak, A., A. King, and T. Lane, 2023: The link between the Madden-Julian Oscillation and rainfall trends in northwest Australia. *Geophys. Res. Lett.*, **50**, e2022GL101799, <https://doi.org/10.1029/2022GL101799>.
- Bowman, D., 2002: The Australian summer monsoon: A biogeographic perspective. *Aust. Geogr. Stud.*, **40**, 261–277, <https://doi.org/10.1111/1467-8470.00179>.
- Brown, J. R., A. F. Moise, R. Colman, and H. Zhang, 2016: Will a warmer world mean a wetter or drier Australian monsoon? *J. Climate*, **29**, 4577–4596, <https://doi.org/10.1175/JCLI-D-15-0695.1>.
- Cai, W., T. Cowan, A. Sullivan, J. Ribbe, and G. Shi, 2011: Are anthropogenic aerosols responsible for the northwest Australia summer rainfall increase? A CMIP3 perspective and implications. *J. Climate*, **24**, 2556–2564, <https://doi.org/10.1175/2010JCLI3832.1>.
- Cao, J., H. Wang, B. Wang, H. Zhao, C. Wang, and X. Zhu, 2022a: Higher sensitivity of Northern Hemisphere monsoon to anthropogenic aerosol than greenhouse gases. *Geophys. Res. Lett.*, **49**, e2022GL100270, <https://doi.org/10.1029/2022GL100270>.
- , —, H. Zhao, B. Wang, L. Wu, and C. Wang, 2022b: Reversed and comparable climate impacts from historical anthropogenic aerosol and GHG on global-scale tropical cyclone genesis potential. *Environ. Res. Lett.*, **17**, 094027, <https://doi.org/10.1088/1748-9326/ac8c5b>.
- , X. Lian, M. Cao, B. Wang, H. Wang, X. Zhu, and H. Zhao, 2023: Wetening of Southern Hemisphere land monsoon during 1901–2014. *J. Climate*, **36**, 8497–8512, <https://doi.org/10.1175/JCLI-D-23-0066.1>.
- Chadwick, R., P. Good, G. Martin, and D. P. Rowell, 2016: Large rainfall changes consistently projected over substantial areas of tropical land. *Nat. Climate Change*, **6**, 177–181, <https://doi.org/10.1038/nclimate2805>.
- Chung, C. T. Y., S. B. Power, J. M. Arblaster, H. A. Rashid, and G. L. Roff, 2014: Nonlinear precipitation response to El Niño and global warming in the Indo-Pacific. *Climate Dyn.*, **42**, 1837–1856, <https://doi.org/10.1007/s00382-013-1892-8>.
- CSIRO, 2020: Unlocking the potential of northern Australia. Accessed 21 April 2023, <https://www.csiro.au/en/research/natural-environment/land/unlocking-northern-australia>.
- Dai, A., 2021: Hydroclimatic trends during 1950–2018 over global land. *Climate Dyn.*, **56**, 4027–4049, <https://doi.org/10.1007/s00382-021-05684-1>.
- Dey, R., S. C. Lewis, and N. J. Abram, 2019: Investigating observed northwest Australian rainfall trends in Coupled Model Intercomparison Project Phase 5 detection and attribution experiments. *Int. J. Climatol.*, **39**, 112–127, <https://doi.org/10.1002/joc.5788>.
- Drosowsky, W., 1996: Variability of the Australian summer monsoon at Darwin: 1957–1992. *J. Climate*, **9**, 85–96, [https://doi.org/10.1175/1520-0442\(1996\)009<0085:VOTASM>2.0.CO;2](https://doi.org/10.1175/1520-0442(1996)009<0085:VOTASM>2.0.CO;2).
- Eyring, V., S. Bony, G. A. Meehl, C. A. Senior, B. Stevens, R. J. Stouffer, and K. E. Taylor, 2016: Overview of the Coupled

- Model Intercomparison Project Phase 6 (CMIP6) experimental design and organization. *Geosci. Model Dev.*, **9**, 1937–1958, <https://doi.org/10.5194/gmd-9-1937-2016>.
- Fahrenbach, N. L. S., and M. A. Bollasina, 2023: Hemispheric-wide climate response to regional COVID-19-related aerosol emission reductions: The prominent role of atmospheric circulation adjustments. *Atmos. Chem. Phys.*, **23**, 877–894, <https://doi.org/10.5194/acp-23-877-2023>.
- Frederiksen, C. S., and S. Grainger, 2015: The role of external forcing in prolonged trends in Australian rainfall. *Climate Dyn.*, **45**, 2455–2468, <https://doi.org/10.1007/s00382-015-2482-8>.
- Freund, M., B. J. Henley, D. J. Karoly, K. J. Allen, and P. J. Baker, 2017: Multi-century cool- and warm-season rainfall reconstructions for Australia's major climatic regions. *Climate Past*, **13**, 1751–1770, <https://doi.org/10.5194/cp-13-1751-2017>.
- Gadgil, S., 2018: The monsoon system: Land-sea breeze or the ITCZ? *J. Earth Syst. Sci.*, **127** (1), 1, <https://doi.org/10.1007/s12040-017-0916-x>.
- Gutiérrez, J. M., and Coauthors, 2021a: Atlas. *Climate Change 2021: The Physical Science Basis*, V. Masson-Delmotte et al., Eds., Cambridge University Press, 1927–2058, <https://doi.org/10.1017/9781009157896.021>.
- , and Coauthors, 2021b: Annex II: Models. *Climate Change 2021: The Physical Science Basis*, V. Masson-Delmotte et al., Eds., Cambridge University Press, 2087–2138, <https://doi.org/10.1017/9781009157896.016>.
- Hadley Centre for Climate Prediction and Research, 2007: HadISST1.1—Global monthly mean gridded SSTs (1870–2015). NCAS British Atmospheric Data Centre, accessed 1 April 2020, <https://catalogue.ceda.ac.uk/uuid/542291c0956a3e4ea2c5085f1a31b94a>.
- Harris, I., T. J. Osborn, P. Jones, and D. Lister, 2020: Version 4 of the CRU TS monthly high-resolution gridded multivariate climate dataset. *Sci. Data*, **7**, 109, <https://doi.org/10.1038/s41597-020-0453-3>.
- Heidemann, H., J. Ribbe, T. Cowan, B. Henley, C. Pudmenzky, R. Stone, and D. H. Cobon, 2022: The influence of interannual and decadal Indo-Pacific sea surface temperature variability on Australian monsoon rainfall. *J. Climate*, **35**, 425–444, <https://doi.org/10.1175/JCLI-D-21-0264.1>.
- , T. Cowan, B. J. Henley, J. Ribbe, M. Freund, and S. Power, 2023: Variability and long-term change in Australian monsoon rainfall: A review. *Wiley Interdiscip. Rev.: Climate Change*, **14**, e823, <https://doi.org/10.1002/wcc.823>.
- Held, I. M., and B. J. Soden, 2006: Robust responses of the hydrological cycle to global warming. *J. Climate*, **19**, 5686–5699, <https://doi.org/10.1175/JCLI3990.1>.
- Hoesly, R. M., and Coauthors, 2018: Historical (1750–2014) anthropogenic emissions of reactive gases and aerosols from the Community Emissions Data System (CEDS). *Geosci. Model Dev.*, **11**, 369–408, <https://doi.org/10.5194/gmd-11-369-2018>.
- Hwang, Y.-T., D. M. W. Frierson, and S. M. Kang, 2013: Anthropogenic sulfate aerosol and the southward shift of tropical precipitation in the late 20th century. *Geophys. Res. Lett.*, **40**, 2845–2850, <https://doi.org/10.1002/grl.50502>.
- Jones, D. A., W. Wang, and R. Fawcett, 2009: High-quality spatial climate data-sets for Australia. *Aust. Meteor. Ocean*, **58**, 233–248, <https://doi.org/10.22499/2.5804.003>.
- Knutson, T. R., and F. Zeng, 2018: Model assessment of observed precipitation trends over land regions: Detectable human influences and possible low bias in model trends. *J. Climate*, **31**, 4617–4637, <https://doi.org/10.1175/JCLI-D-17-0672.1>.
- Lewinschal, A., A. M. L. Ekman, and H. Kornich, 2013: The role of precipitation in aerosol-induced changes in Northern Hemisphere wintertime stationary waves. *Climate Dyn.*, **41**, 647–661, <https://doi.org/10.1007/s00382-012-1622-7>.
- Li, C., and Coauthors, 2017: India is overtaking China as the world's largest emitter of anthropogenic sulfur dioxide. *Sci. Rep.*, **7**, 14304, <https://doi.org/10.1038/s41598-017-14639-8>.
- Lin, Z., and Y. Li, 2012: Remote influence of the tropical Atlantic on the variability and trend in North West Australia summer rainfall. *J. Climate*, **25**, 2408–2420, <https://doi.org/10.1175/JCLI-D-11-00020.1>.
- Lisonbee, J., J. Ribbe, and M. Wheeler, 2019: Defining the north Australian monsoon onset: A systematic review. *Prog. Phys. Geog.*, **44**, 398–418, <https://doi.org/10.1177/0309133319881107>.
- Liu, Z., Y. Ming, L. Wang, M. Bollasina, M. Luo, N.-C. Lau, and S. H.-L. Yim, 2019: A model investigation of aerosol-induced changes in the East Asian winter monsoon. *Geophys. Res. Lett.*, **46**, 10 186–10 195, <https://doi.org/10.1029/2019GL084228>.
- Matsueda, M., and T. N. Palmer, 2011: Accuracy of climate change predictions using high resolution simulations as surrogates of truth. *Geophys. Res. Lett.*, **38**, L05803, <https://doi.org/10.1029/2010GL046618>.
- McKeon, G., G. Stone, D. Ahrens, J. Carter, D. Cobon, S. Irvine, and J. Syktus, 2021: Queensland's multi-year wet and dry periods: Implications for grazing enterprises and pasture resources. *Rangeland J.*, **43**, 121–142, <https://doi.org/10.1071/RJ20089>.
- Ming, Y., and V. Ramaswamy, 2009: Nonlinear climate and hydrological responses to aerosol effects. *J. Climate*, **22**, 1329–1339, <https://doi.org/10.1175/2008JCLI2362.1>.
- Myhre, G., and Coauthors, 2013: Radiative forcing of the direct aerosol effect from AeroCom Phase II simulations. *Atmos. Chem. Phys.*, **13**, 1853–1877, <https://doi.org/10.5194/acp-13-1853-2013>.
- , and Coauthors, 2017a: Multi-model simulations of aerosol and ozone radiative forcing due to anthropogenic emission changes during the period 1990–2015. *Atmos. Chem. Phys.*, **17**, 2709–2720, <https://doi.org/10.5194/acp-17-2709-2017>.
- , and Coauthors, 2017b: PDRMIP: A Precipitation Driver and Response Model Intercomparison Project—Protocol and preliminary results. *Bull. Amer. Meteor. Soc.*, **98**, 1185–1198, <https://doi.org/10.1175/BAMS-D-16-0019.1>.
- Narsey, S. Y., J. R. Brown, R. A. Colman, F. Delage, S. B. Power, A. F. Moise, and H. Zhang, 2020: Climate change projections for the Australian monsoon from CMIP6 models. *Geophys. Res. Lett.*, **47**, e2019GL086816, <https://doi.org/10.1029/2019GL086816>.
- Nicholls, N., W. Drosowsky, and B. Lavery, 1997: Australian rainfall variability and change. *Weather*, **52**, 66–72, <https://doi.org/10.1002/j.1477-8696.1997.tb06274.x>.
- O'Gorman, P. A., R. P. Allan, M. P. Byrne, and M. Previdi, 2012: Energetic constraints on precipitation under climate change. *Surv. Geophys.*, **33**, 585–608, <https://doi.org/10.1007/s10712-011-9159-6>.
- Persad, G. G., 2023: The dependence of aerosols' global and local precipitation impacts on the emitting region. *Atmos. Chem. Phys.*, **23**, 3435–3452, <https://doi.org/10.5194/acp-23-3435-2023>.
- , Y. Ming, Z. Shen, and V. Ramaswamy, 2018: Spatially similar surface energy flux perturbations due to greenhouse gases and aerosols. *Nat. Commun.*, **9**, 3247, <https://doi.org/10.1038/s41467-018-05735-y>.
- Power, S., F. Tseitkin, V. Mehta, B. Lavery, S. Torok, and N. Holbrook, 1999: Decadal climate variability in Australia

- during the twentieth century. *Int. J. Climatol.*, **19**, 169–184, [https://doi.org/10.1002/\(SICI\)1097-0088\(199902\)19:2<169:AJD-JOC356>3.0.CO;2-Y](https://doi.org/10.1002/(SICI)1097-0088(199902)19:2<169:AJD-JOC356>3.0.CO;2-Y).
- Qureshi, M. E., M. A. Hanjra, and J. Ward, 2013: Impact of water scarcity in Australia on global food security in an era of climate change. *Food Policy*, **38**, 136–145, <https://doi.org/10.1016/j.foodpol.2012.11.003>.
- Ren, L., P. Arkin, T. M. Smith, and S. S. P. Shen, 2013: Global precipitation trends in 1900–2005 from a reconstruction and coupled model simulations. *J. Geophys. Res. Atmos.*, **118**, 1679–1689, <https://doi.org/10.1002/jgrd.50212>.
- Rodgers, K. B., and Coauthors, 2021: Ubiquity of human-induced changes in climate variability. *Earth Syst. Dyn.*, **12**, 1393–1411, <https://doi.org/10.5194/esd-12-1393-2021>.
- Rotstayn, L. D., and Coauthors, 2007: Have Australian rainfall and cloudiness increased due to the remote effects of Asian anthropogenic aerosols? *J. Geophys. Res.*, **112**, D09202, <https://doi.org/10.1029/2006JD007712>.
- , S. J. Jeffrey, M. A. Collier, S. M. Dravitzki, A. C. Hirst, J. I. Syktus, and K. K. Wong, 2012: Aerosol- and greenhouse gas-induced changes in summer rainfall and circulation in the Australasian region: A study using single-forcing climate simulations. *Atmos. Chem. Phys.*, **12**, 6377–6404, <https://doi.org/10.5194/acp-12-6377-2012>.
- Roxy, M. K., P. Dasgupta, M. J. McPhaden, T. Suematsu, C. Zhang, and D. Kim, 2019: Twofold expansion of the Indo-Pacific warm pool warps the MJO life cycle. *Nature*, **575**, 647–651, <https://doi.org/10.1038/s41586-019-1764-4>.
- Samset, B. H., and Coauthors, 2016: Fast and slow precipitation responses to individual climate forcings: A PDRMIP multimodel study. *Geophys. Res. Lett.*, **43**, 2782–2791, <https://doi.org/10.1002/2016GL068064>.
- , M. T. Lund, M. Bollasina, G. Myhre, and L. Wilcox, 2019: Emerging Asian aerosol patterns. *Nat. Geosci.*, **12**, 582–584, <https://doi.org/10.1038/s41561-019-0424-5>.
- Schneider, U., A. Becker, P. Finger, A. Meyer-Christoffer, and M. Ziese, 2022: GPCC full data monthly product version 2022 at 0.5°: Monthly land-surface precipitation from rain-gauges built on GTS-based and historical data. Accessed 1 April 2020, [https://doi.org/10.5676/DWD\\_GPCC/FD\\_M\\_V2022\\_050](https://doi.org/10.5676/DWD_GPCC/FD_M_V2022_050).
- Seager, R., and N. Naik, 2012: A mechanisms-based approach to detecting recent anthropogenic hydroclimate change. *J. Climate*, **25**, 236–261, <https://doi.org/10.1175/JCLI-D-11-00056.1>.
- , —, and G. A. Vecchi, 2010: Thermodynamic and dynamic mechanisms for large-scale changes in the hydrological cycle in response to global warming. *J. Climate*, **23**, 4651–4668, <https://doi.org/10.1175/2010JCLI3655.1>.
- Shi, G., W. Cai, T. Cowan, J. Ribbe, L. Rotstayn, and M. Dix, 2008: Variability and trend of North West Australia rainfall: Observations and coupled climate modeling. *J. Climate*, **21**, 2938–2959, <https://doi.org/10.1175/2007JCLI1908.1>.
- Shiogama, H., D. A. Stone, T. Nagashima, T. Nozawa, and S. Emori, 2013: On the linear additivity of climate forcing–response relationships at global and continental scales. *Int. J. Climatol.*, **33**, 2542–2550, <https://doi.org/10.1002/joc.3607>.
- Shonk, J. K. P., A. G. Turner, A. Chevuturi, L. J. Wilcox, A. J. Dittus, and E. Hawkins, 2020: Uncertainty in aerosol radiative forcing impacts the simulated global monsoon in the 20th century. *Atmos. Chem. Phys.*, **20**, 14903–14915, <https://doi.org/10.5194/acp-20-14903-2020>.
- Slivinski, L. C., and Coauthors, 2019: NOAA-CIRES-DOE twentieth century reanalysis version 3. Research Data Archive at the National Center for Atmospheric Research, Computational and Information Systems Laboratory, accessed 1 April 2020, <https://doi.org/10.5065/H93G-WS83>.
- Suppiah, R., 1992: The Australian summer monsoon: A review. *Prog. Phys. Geogr.*, **16**, 283–318, <https://doi.org/10.1177/030913339201600302>.
- Szopa, S., and Coauthors, 2021: Short-lived climate forcings. *Climate Change 2021: The Physical Science Basis*, V. Masson-Delmotte et al., Eds., Cambridge University Press, 817–922.
- Taschetto, A. S., and M. H. England, 2009: An analysis of late twentieth century trends in Australian rainfall. *Int. J. Climatol.*, **29**, 791–807, <https://doi.org/10.1002/joc.1736>.
- Twomey, S., 1977: Influence of pollution on shortwave albedo of clouds. *J. Atmos. Sci.*, **34**, 1149–1152, [https://doi.org/10.1175/1520-0469\(1977\)034<1149:TIOPOT>2.0.CO;2](https://doi.org/10.1175/1520-0469(1977)034<1149:TIOPOT>2.0.CO;2).
- Vecchi, G. A., and B. J. Soden, 2007: Global warming and the weakening of the tropical circulation. *J. Climate*, **20**, 4316–4340, <https://doi.org/10.1175/JCLI4258.1>.
- , —, A. T. Wittenberg, I. M. Held, A. Leetmaa, and M. J. Harrison, 2006: Weakening of tropical Pacific atmospheric circulation due to anthropogenic forcing. *Nature*, **441**, 73–76, <https://doi.org/10.1038/nature04744>.
- Wang, C., D. Kim, A. M. L. Ekman, M. C. Barth, and P. J. Rasch, 2009: Impact of anthropogenic aerosols on Indian summer monsoon. *Geophys. Res. Lett.*, **36**, L21704, <https://doi.org/10.1029/2009GL040114>.
- Westervelt, D. M., Y. You, X. Li, M. Ting, D. E. Lee, and Y. Ming, 2020: Relative importance of greenhouse gases, sulfate, organic carbon, and black carbon aerosol for South Asian monsoon rainfall changes. *Geophys. Res. Lett.*, **47**, e2020GL088363, <https://doi.org/10.1029/2020GL088363>.
- Wilcox, L. J., N. Dunstone, A. Lewinschal, M. Bollasina, A. M. L. Ekman, and E. J. Highwood, 2019: Mechanisms for a remote response to Asian anthropogenic aerosol in boreal winter. *Atmos. Chem. Phys.*, **19**, 9081–9095, <https://doi.org/10.5194/acp-19-9081-2019>.
- Xian, T., J. Xia, W. Wei, Z. Zhang, R. Wang, L.-P. Wang, and Y.-F. Ma, 2021: Is Hadley cell expanding? *Atmosphere*, **12**, 1699, <https://doi.org/10.3390/atmos12121699>.
- Xie, S.-P., B. Lu, and B. Xiang, 2013: Similar spatial patterns of climate responses to aerosol and greenhouse gas changes. *Nat. Geosci.*, **6**, 828–832, <https://doi.org/10.1038/ngeo1931>.
- Zhou, Z.-Q., and S.-P. Xie, 2015: Effects of climatological model biases on the projection of tropical climate change. *J. Climate*, **28**, 9909–9917, <https://doi.org/10.1175/JCLI-D-15-0243.1>.